Politecnico di Torino

Politecnico di Torino

Master's Degree in Automotive Engineering

A.Y. 2024/2025

Graduation Session October 2025

Modelling of an Anti–Intrusion Plate in CFRP for a Formula Student Vehicle

Supervisors:

Prof. Davide Salvatore Paolino
Prof. Andrea Tonoli
Prof. Alberto Ciampaglia
Prof. Raffaele Ciardiello

Candidate:

Riccardo Signorino

Abstract

This thesis investigates the development of structural solutions for the Impact Assembly of Formula SAE vehicles, with particular focus to the Anti-Intrusion Plate, a critical component for the safety designed to protect the driver during frontal impacts.

After an experimental characterisation of composite materials through tensile and in-plane shear tests, the mechanical responses were modelled using LS-DYNA to support numerical analysis.

The first phase reproduced the failure mechanisms observed in a sandwich-type AIP with a honeycomb core, tested in conjunction with an origami-shaped CFRP impact attenuator. Experimental tests and finite element simulations demonstrated that the sandwich configuration is inadequate under localised loading, leading to premature structural collapse..

To address these limitations, the study explored an alternative monolithic configuration entirely made of CFRP. Drop-weight impact tests and numerical simulations confirmed that this solution satisfies Formula SAE safety requirements while achieving significant weight reduction.

Overall, the work highlights how an integrated experimental–numerical approach enables the design of innovative, lightweight, and high-performance anti-intrusion systems, paving the way for further optimisation of composite layup strategies in motorsport applications.

Contents

List of Tables

List of Figures

List of Acronyms

AIP	Anti-Intrusion Plate
CFRP	Carbon Fibre Reinforced Polymer
FBH	Front Bulkhead
FEM	Finite Element Method
FSAE	Formula SAE
GFRP	Glass Fibre Reinforced Polymer
IA	Impact Attenuator
IPS	In-Plane Shear
SAE	Society of Automotive Engineers
SES	Structural Equivalency Spreadsheet

Chapter 1

Introduction

1.1 Formula SAE - Overview and Competition Structure

Figure 1.1: Teams lineup at the 2024 Formula Student Austria (FSA) competition.

Formula SAE (FSAE) is an international engineering design competition organised by SAE International [1], in which student teams from universities around the world conceive, design, manufacture, and validate a prototype single-seater race car. The event aims to replicate a professional motorsport environment and provide students with practical experience in automotive engineering, teamwork, and project management. Each team is required to develop a car that complies with a detailed set of technical and safety regulations defined annually in the Formula

STUDENT rulebook. The competition comprises both static and dynamic events. The static events include cost and manufacturing analysis, business presentation, and design evaluation. The dynamic events assess the vehicle's on-track performance through acceleration, skidpad, autocross, and endurance trials.

Crashworthiness, in particular, represents a central safety concern. To demonstrate compliance with frontal crash regulations, teams must design a crash structure, known as the *Impact Assembly*, capable of absorbing impact energy and preventing intrusion into the cockpit, thereby ensuring driver protection.

1.2 Impact Assembly

1.2.1 Definition and Function

The *Impact Assembly* is a critical structural subsystem positioned at the front of a FORMULA SAE vehicle. Its primary function is to protect the driver during frontal collision by absorbing kinetic energy and preventing intrusion into the cockpit.

The *Impact Assembly* typically consists of two key elements:

- **Impact Attenuator (IA)**: "A deformable, energy absorbing device located forward of the *Front Bulkhead*" [2], as defined in rule T1.1.8 of the FSAE 2025 rulebook.

- **Anti-Intrusion Plate (AIP)**: A rigid panel mounted between the IA and the *Front Bulkhead*, designed to prevent the penetration of objects into the driver cell.

The *Front Bulkhead* of a FORMULA STUDENT vehicle is defined as follows:

- **Front Bulkhead (FBH)**: "A planar structure that defines the forward plane of the chassis and provides protection for the driver's feet (In front view, together with the *Anti-Intrusion Plate* (AIP), covers the driver's feet)." [2], according to rule T1.1.5.

These components must work synergistically to ensure that the forces generated during impact are adequately managed and that the integrity of the survival cell is preserved.

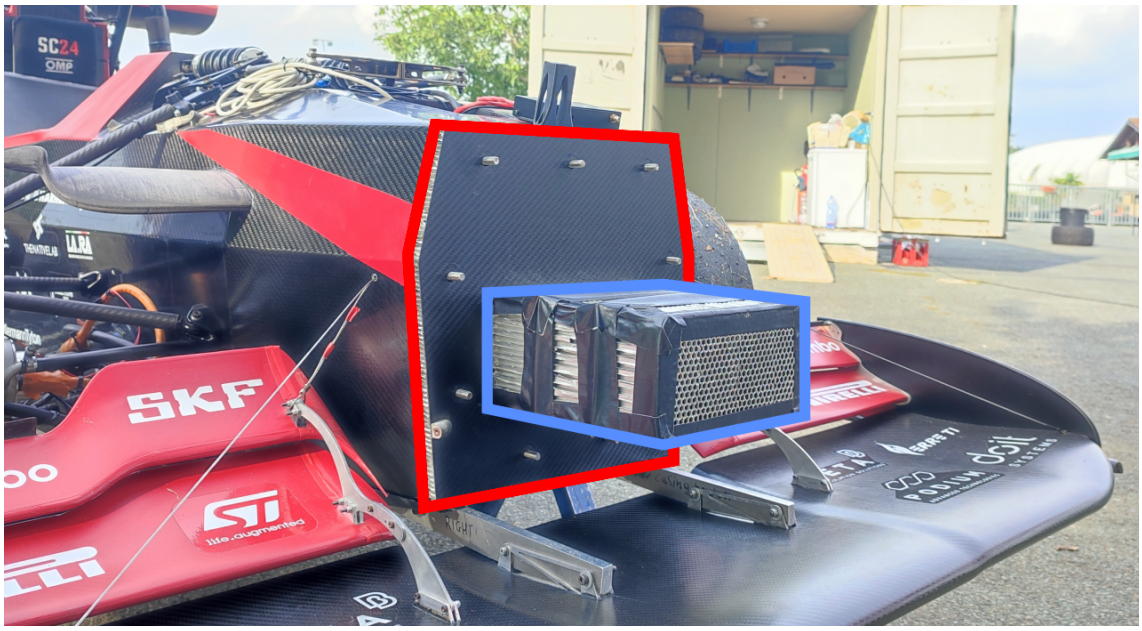

Figure 1.2: Detail of the Squadra Corse PoliTo 2024 vehicle's AIP (red outline) and IA (blue outline) components.

1.2.2 Regulatory Requirements

The safety of the driver in a frontal impact is guaranteed through a set of precise requirements for the IA and the AIP, defined in Sections T3.16 to T3.19 of the 2025 Formula Student rules [2]. Among the topics covered by these rules are the geometry, attachment methods, and testing procedure for the Impact Assembly.

General requirements (T3.16). Each vehicle must be equipped with an *Impact Assembly*, consisting of both an IA and an AIP. The main prescriptions are:

- The IA must be mounted forward of the front bulkhead, with minimum dimensions of 100 mm in height and 200 mm in width, extending at least 200 mm ahead of the bulkhead.
- The IA volume (100 mm × 200 mm × 200 mm) must not be positioned more than 350 mm above the ground.
- The IA must be securely attached directly to the AIP, designed with a closed front section, and must not be part of the non-structural bodywork.
- Attachment methods must ensure adequate load paths also under off-axis impacts. If adhesives are used, they must withstand at least 60 kN in any direction; bolted connections must use a minimum of four 8 mm metric grade 8.8 bolts.

Crash test requirements (T3.18). For non-standard IAs (see Section 1.2.3), physical validation by crash testing is compulsory. The IA assembly must satisfy the following conditions when a 300 kg mass impacts a rigid, non-yielding barrier at $7\,\mathrm{m\,s^{-1}}$:

- **Energy absorption:** at least 7350 J.
- **Deceleration limits:** average deceleration ≤ 20 g, peak deceleration ≤ 40 g.
- **AIP integrity:** no permanent deflection greater than 25 mm.

Further conditions apply to the test setup:

- The IA must be mounted to the AIP using the actual attachment system intended for the car.
- The test fixture must represent the stiffness and geometry of the vehicle's primary structure; when alternative materials are used for the AIP (e.g. composites), the fixture must replicate the same layup and joining method.
- A clearance of at least 50 mm must be maintained behind the AIP.

1.2.3 State of the Art

The Formula SAE rulebook defines a standard *Impact Assembly* configuration that, according to rule T3.16.7, does not require physical testing. This configuration consists of either a 1.5 mm thick steel plate or a 4 mm thick aluminium plate acting as the AIP, combined with the prescribed 200 mm × 100 mm × 203 mm single-piece, pre-crushed aluminium honeycomb IA specified in the FSAE technical drawing [3] reported in Figure 1.3.

Aluminium honeycomb has become a reference energy-absorbing material in crashworthiness applications thanks to its nearly elastic-perfectly plastic response and the associated constant plateau stress during crushing, which ensures stable and predictable energy absorption [4].

While the standard solution simplifies compliance with FSAE safety requirements, it is relatively heavier; thus, many teams design custom crash structures tailored to their vehicle performance objectives.

In recent years, *Squadra Corse PoliTo* has adopted an alternative configuration consisting of a pre-crushed modular aluminium honeycomb IA combined with a sandwich-structured AIP (see Figures 1.2 and 1.4), designed to be lighter than the standard options while ensuring driver safety as well.

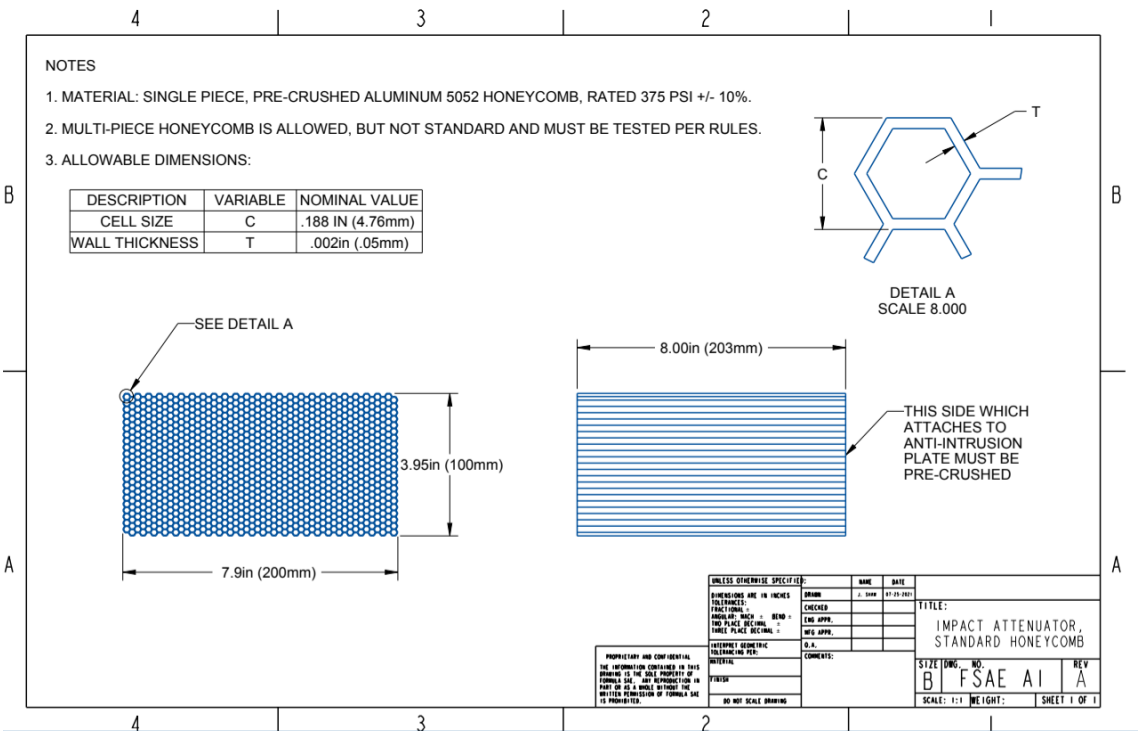

Figure 1.3: Standard configuration of the Impact Attenuator.

In this solution, the IA was composed of three aluminium 1/4-5052-0.0025 5.2 pcf modules, each with an initial height of 80 mm, pre-crushed to 70 mm. The pre-crush of each module aimed at mitigating the initial force peaks prior to the onset of honeycomb cell buckling. To allow proper gluing between the modules themselves, two GFRP divisors were placed at the interfaces.

The AIP consisted of symmetric CFRP skins with layup 0T/0U/90U/45U/-45U/0U/90U (where T denotes the high-strength T800 twill 2×2 prepreg characterised in Chapter 2, while U denotes the high-modulus M46J unidirectional prepreg, whose properties are reported in Table 3.1) and a 20 mm thick aluminium honeycomb core 1/8-5052-0.0015 6.1 pcf.

This design has been successfully implemented and validated in previous seasons, ensuring full compliance with FSAE safety standards.

Despite this success, the team identified the need to further reduce the weight of the crash structure. This led to the investigation of a new concept based on a full origami-designed CFRP IA (see Figure 1.5b), as proposed and analysed in the thesis by Patruno [5].

The feasibility of such a design is supported by several studies demonstrating the capability of composite crash structures to absorb energy efficiently. In particular, the study by Ciampaglia et al. [6] confirmed the possibility of control-

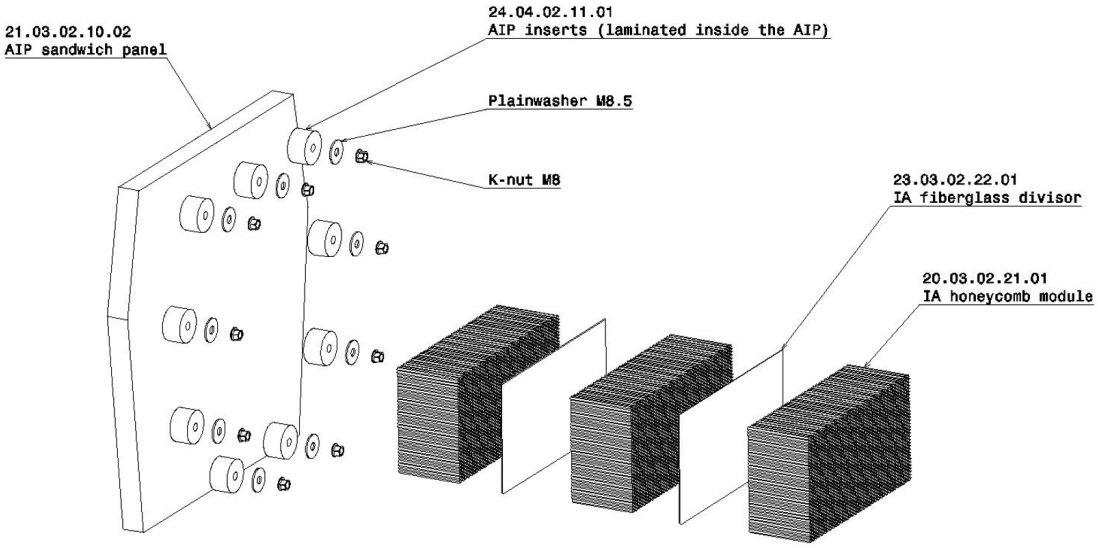

Figure 1.4: Exploded Modular Impact Assembly view.

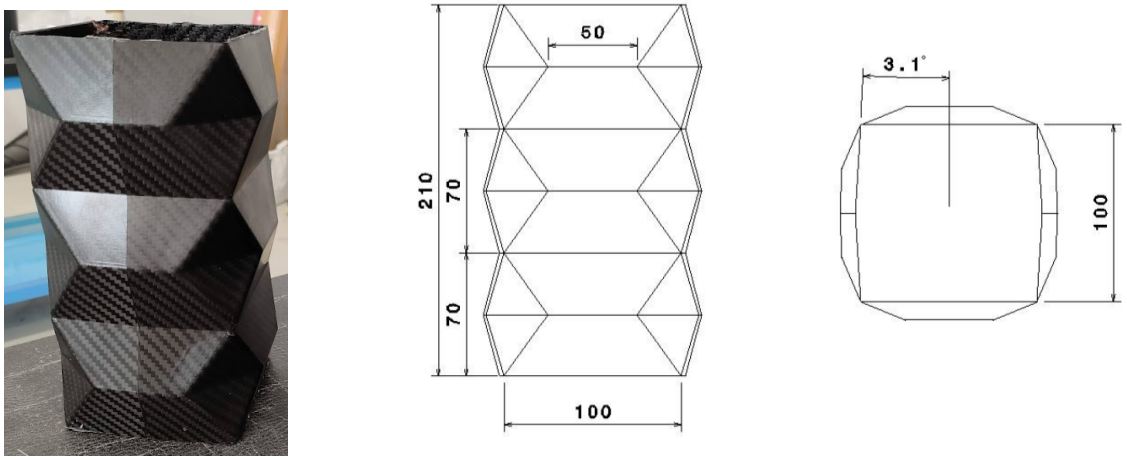

(a) (b)

Figure 1.5: Origami CFRP IA design by Patruno.

ling both the absorbed energy and the peak force by adjusting the geometrical parameters of an origami-shaped crash box without affecting the weight, encouraging the team to follow this path. The literature on the modelling of composite crash properties has rapidly evolved, offering reliable methods to reproduce progressive failure through advanced material models such as LS-DYNA `MAT_054 (ENHANCED_COMPOSITE_DAMAGE)` [7, 8]. In addition, advanced methodologies for the automated identification of material parameters from crash tests have been proposed, allowing predictive simulations of composite absorbers while minimizing the need for extensive physical testing. [9].

Building upon these findings, the design proposed by Patruno achieved significant weight reduction while maintaining adequate energy absorption capabilities. However, it introduced a critical limitation: the significant smaller contact area between the IA and the AIP. Unlike aluminium honeycomb IA that distribute loads over a broad surface, the CFRP origami design concentrates impact forces in a localized region.

Such concentrated loading is incompatible with the mechanical behaviour of sandwich structures, which are optimized to resist distributed pressure fields. Consequently, during frontal crash conditions, the sandwich AIP experienced interlaminar shear failure initiating at the IA–AIP interface.

The crash, conducted according to FSAE rulebook specifications using an instrumented sled accelerated to the prescribed impact speed, confirmed the weakness. As shown in Figure 1.6, the IA penetrated the AIP panel, clearly demonstrating the inadequacy of the sandwich architecture for the origami configuration.

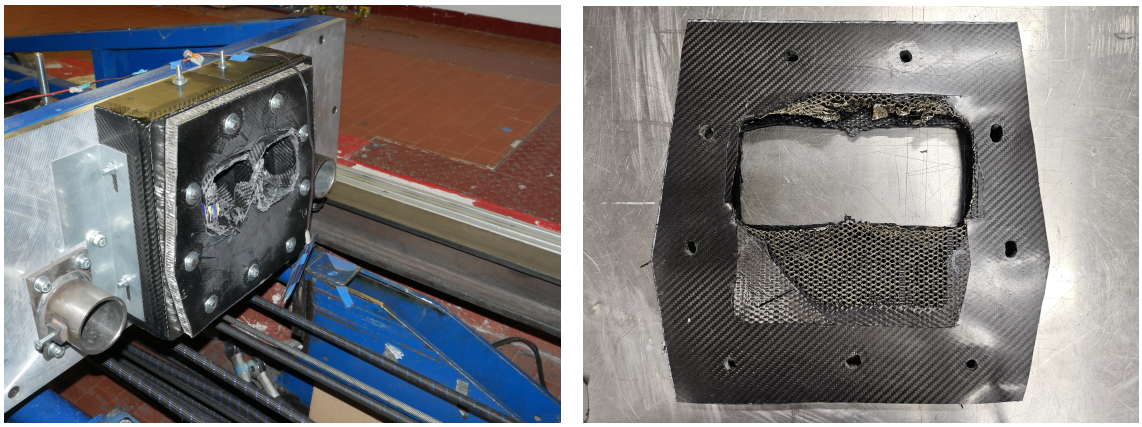

(a) (b)

Figure 1.6: Outcome of the 2024 crash test for the origami design. In (a) the impact assembly still mounted on the sled system immediately after the test; in (b) the AIP panel perforated with a clean cut produced by the IA.

This outcome prompted the investigation of alternative AIP structural concepts, including the fully monolithic composite configuration presented in this work. During the IA development phase, considerable effort had been devoted to refining the FEM model of the attenuator, whereas the AIP was modelled with less detail. This imbalance led to an overestimation of the panel's structural adequacy—an assumption later disproved by the crash test results.

Consequently, the study began with the development of an improved numerical model of the sandwich AIP to assess whether a more accurate representation could have anticipated the observed failure. The new model was calibrated using the perimeter shear tests required by the FSAE *Structural Equivalency Spreadsheet* (SES). Although static testing does not fully capture dynamic crash behaviour, this approach proved fast, cost-effective, and highly informative for preliminary assessment. The simulation successfully reproduced the panel's failure mode, providing valuable insight into the limitations of the original design.

Chapter 2

Material Characterization

The composite material selected for the design of the AIP is the GG200T(T800)-DT120-42 from Delta Preg, a 2×2 twill-weave carbon-fibre fabric pre-impregnated with a thermosetting epoxy resin. This prepreg system combines high-strength carbon fibres with a toughened resin matrix, making it suitable for structural applications requiring both stiffness and impact resistance.

The T800 carbon fibre filament belongs to the family of intermediate modulus, high-strength fibres (see Figure 2.1), offering an excellent balance between tensile properties and weight reduction [10]. Its use is widespread in the aerospace and motorsport sectors where performance to weight ratio is critical.

The 2×2 twill weave architecture enhances the drapability of the fabric, allowing it to conform to complex geometries and tridimensional surfaces, while preserving good mechanical performance. Improves handling and reduces the risk of fibre distortion during lay-up.

The DT120 epoxy resin is a high-viscosity, highly toughened thermosetting matrix designed for autoclave vacuum bag curing within a flexible processing window ranging from 100 °C to 135 °C [11]. Its rheological profile ensures adequate resin flow under vacuum conditions, while the toughness of the system provides high energy absorption and impact resistance.

To properly define the material input for the finite element model, tensile and in-plane shear (IPS) characterisation tests were carried out in accordance with the ASTM D3039 [12] and ASTM D3518 [13] standards.

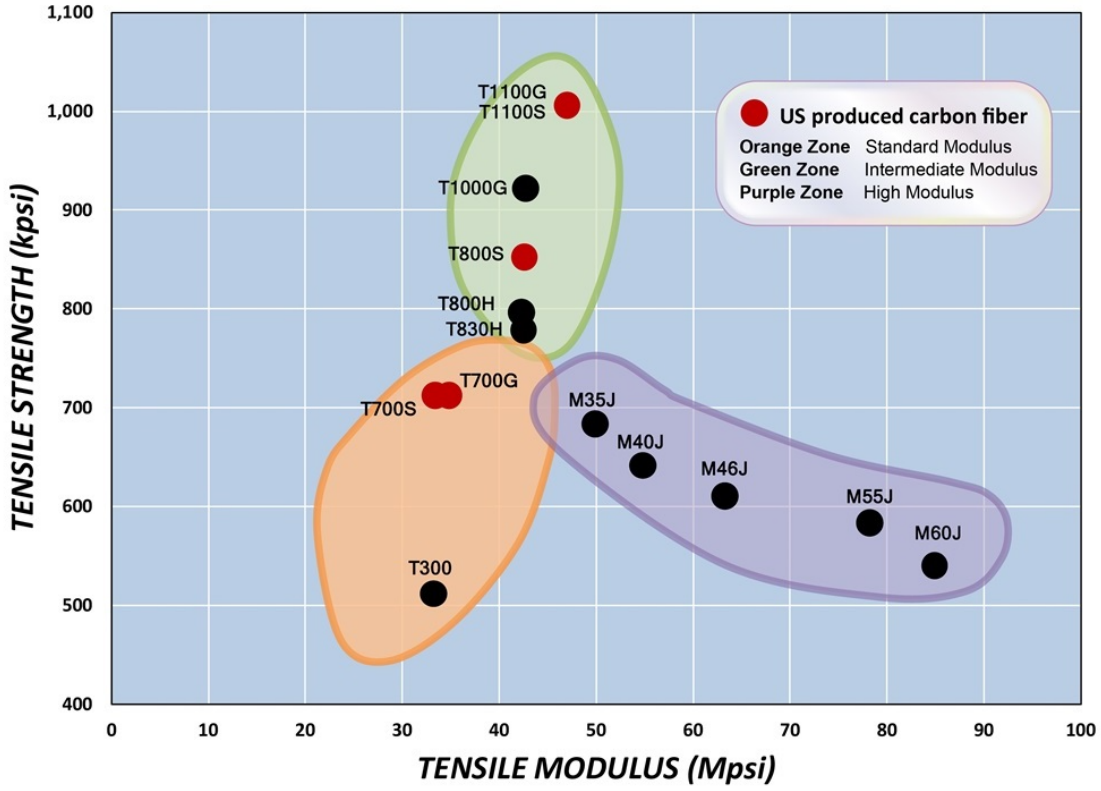

Figure 2.1: Chart representing tensile strength and tensile modulus for different grades of carbon fibres. The orange, green, and purple regions correspond to standard, intermediate, and high modulus fibres, respectively.

2.1 Specimens Production

The specimens for all tests were produced following a consistent procedure, obtained form a flat laminate manufactured by autoclave curing. The stacking sequence was first laid on a pre-detached support plate. Once the plies were arranged, a second detached plate was placed on top of the stack to prevent surface irregularities that could arise from vacuum bagging. The assembly was then sealed in a vacuum bag and subjected to autoclave curing process under a pressure of 4 bar and a temperature of 130 °C for 90 min. After curing, the laminate was cut to the desired specimen dimensions using water-jet cutting.

The characteristics of the tested specimens are summarised in Sections 2.2 and 2.3. In particular, Tables 2.1, 2.3, and 2.4 report the specimen sets. The specimens for tensile tests are denoted by the letter *T*, those used for shear strength by *SS*, and those employed for shear modulus by *SM*.

2.2 Tensile Test

Tensile properties were characterised through uniaxial tests performed on specimens with a $[0°]_{12}$ layup, in accordance with the ASTM D3039 standard [12]. The experiments were carried out by applying an initial preload of 5 kN to stabilise the specimens before the actual loading. Axial strain was monitored using a clip-on extensometer with a gauge length of 25 mm, ensuring accurate determination of the elastic modulus.

Specimen	**Thickness** (mm)	**Length** (mm)	**Width** (mm)	**Layup**
T1	2.70	250	8.25	$[0°]_{12}$
T2	3.00	250	8.04	$[0°]_{12}$
T3	2.90	250	8.04	$[0°]_{12}$
T4	2.76	250	8.00	$[0°]_{12}$

Table 2.1: Tensile test specimens.

The results in Table 2.2 show that the measured average tensile modulus (62.8 GPa) closely matches the values reported for this type of pre-impregnated material, whereas the average ultimate tensile strength (569 MPa) falls significantly below the expected range.

Specimen	**Modulus** (GPa)	**Strength** (MPa)
T1	65.5	678
T2	57.1	462
T3	62.8	583
T4	65.7	554
Average	62.8	569

Table 2.2: Tensile test results.

2.3 In-Plane Shear Test

The IPS properties of the material were determined in accordance with the ASTM D3518 standard [13], using specimens with a $[\pm 45°]_{10}$ layup. The tests were carried again applying an initial preload of 5 kN to stabilise the specimens before the loading sequence.

Two batches of specimens were produced. The first set was tested to determine the in-plane shear strength, while the second was instrumented with HBM 1-LY48-

3/350 strain gauges aligned both parallel and transverse to the loading direction, in order to evaluate the shear modulus. The results are reported in 2.3 and 2.4.

Specimen	**Thickness** (mm)	**Length** (mm)	**Width** (mm)	**Layup**	**Strength** (MPa)
SS1	2.17	200	24.50	$[\pm 45^\circ]_{10}$	128
SS2	2.32	200	25.15	$[\pm 45^\circ]_{10}$	128
SS3	2.41	200	24.45	$[\pm 45^\circ]_{10}$	136
SS4	2.42	200	25.60	$[\pm 45^\circ]_{10}$	132
SS5	2.36	200	24.70	$[\pm 45^\circ]_{10}$	116
SS6	2.22	200	24.90	$[\pm 45^\circ]_{10}$	133

Table 2.3: IPS test specimens and results for the Strength Series.

Specimen	**Thickness** (mm)	**Length** (mm)	**Width** (mm)	**Layup**	**Shear Modulus** (GPa)
SM1	2.20	200	24.98	$[\pm 45^\circ]_{10}$	3.10
SM2	2.46	200	25.35	$[\pm 45^\circ]_{10}$	2.82
SM3	2.35	200	25.10	$[\pm 45^\circ]_{10}$	2.89
SM4	2.34	200	25.10	$[\pm 45^\circ]_{10}$	3.03

Table 2.4: IPS test specimens and results for the Modulus Series.

The obtained results showed an average shear strength of 129 MPa and an average shear modulus of 2.96 GPa. Both values are consistent with the expected performance of T800/DT120 carbon/epoxy laminates. The failure mode is compatible with the standard specification as shown in 2.2a and 2.2b.

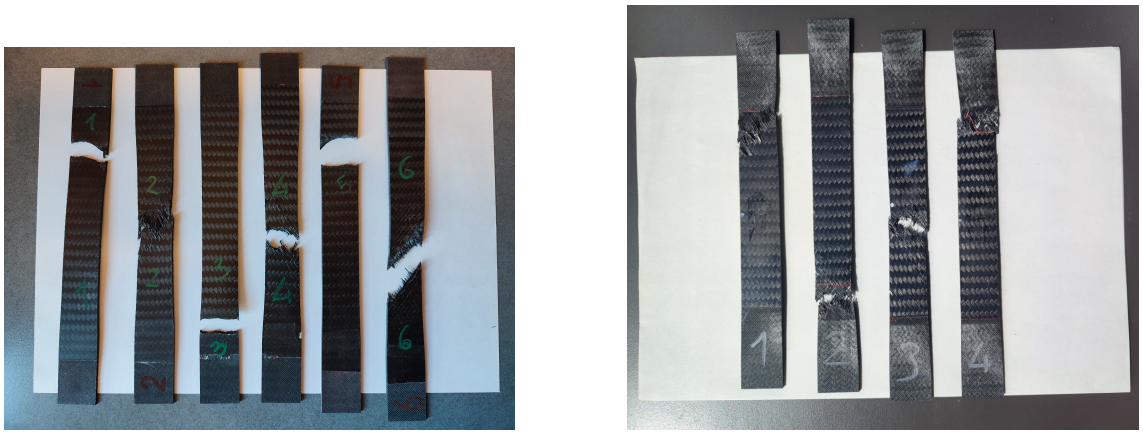

(a) (b)

Figure 2.2: Post-test condition of the IPS specimens: (a) specimens used for the evaluation of in-plane shear strength; (b) specimens used for the determination of the in-plane shear modulus.

2.4 Material Formulations

2.4.1 MAT_054 (Enhanced Composite Damage)

To input the material properties into the solver and to define the mechanical behaviour and failure mechanisms of the CFRP plies, the LS-DYNA progressive-failure model `MAT_054 (ENHANCED_COMPOSITE_DAMAGE)` was used. As described in the LS-DYNA documentation and single-element investigations [8, 14], this formulation models a laminate with a single shell element by treating each ply as a through-thickness integration point and it uses Chang–Chang/Hashin-type criteria.

Ply stress–strain relations. The stress–strain equations used for each ply are:

$$\varepsilon_{11} = \frac{1}{E_1}\left(\sigma_{11} - \nu_{12}\sigma_{22}\right), \tag{2.1}$$

$$\varepsilon_{22} = \frac{1}{E_2}\left(\sigma_{22} - \nu_{21}\sigma_{11}\right), \tag{2.2}$$

$$2\,\varepsilon_{12} = \frac{1}{G_{12}}\,\sigma_{12} + \alpha\,\sigma_{12}^3, \tag{2.3}$$

where E_1, E_2, G_{12} are the in-plane moduli, ν_{12}, ν_{21} are Poisson's ratios, and α is the shear nonlinearity parameter (`ALPH`).[8, 14]

Failure criteria (Chang–Chang / Hashin family). The four mode-specific indices used by the card are:

$$\text{Tensile fiber:} \quad e_f^2 = \left(\frac{\sigma_{11}}{X_T}\right)^2 + \beta\left(\frac{\sigma_{12}}{S_C}\right)^2 - 1, \tag{2.4}$$

$$\text{Compressive fiber:} \quad e_c^2 = \left(\frac{\sigma_{11}}{X_C}\right)^2 - 1, \tag{2.5}$$

$$\text{Tensile matrix:} \quad e_m^2 = \left(\frac{\sigma_{22}}{Y_T}\right)^2 + \left(\frac{\sigma_{12}}{S_C}\right)^2 - 1, \tag{2.6}$$

$$\text{Compressive matrix:} \quad e_d^2 = \left(\frac{\sigma_{22}}{2S_C}\right)^2 + \left[\left(\frac{Y_C}{2S_C}\right)^2 - 1\right]\frac{\sigma_{22}}{Y_C} + \left(\frac{\sigma_{12}}{S_C}\right)^2 - 1, \tag{2.7}$$

with X_T, X_C, Y_T, Y_C the ply strengths in tension and compression, S_C the in-plane shear strength, and β (`BETA`) the shear-weighting in the tensile-fiber mode. A mode is deemed failed when its index is ≥ 0.[8, 14]

Degradation factors. Material degradation can be controlled through the factors `FBRT`, `YCFAC` and `SOFT`, which act as reduction multipliers on the input strengths as

follows:

$$\{X_T, X_C, Y_T, Y_C\}_{\text{reduced}} = \{X_T, X_C, Y_T, Y_C\} \cdot \texttt{SOFT}, \tag{2.8}$$

$$\{X_T\}_{\text{reduced}} = X_T \cdot \texttt{FBRT}, \tag{2.9}$$

$$\{X_C\}_{\text{reduced}} = Y_C \cdot \texttt{YCFAC}. \tag{2.10}$$

[8, 14]

Moreover, when maximum stress is achieved, the `SLIM*` parameters are used to determine the subsequent minimum stress limit.

Element deletion. Ply deletion is activated by strain-based limits via the parameters `DFAILT` (tension), `DFAILC` (compression), `DFAILM` (matrix direction) and `DFAILS` (shear).[8, 14]

Figure 2.3 qualitatively summarises the behaviour of the material formulation [15].

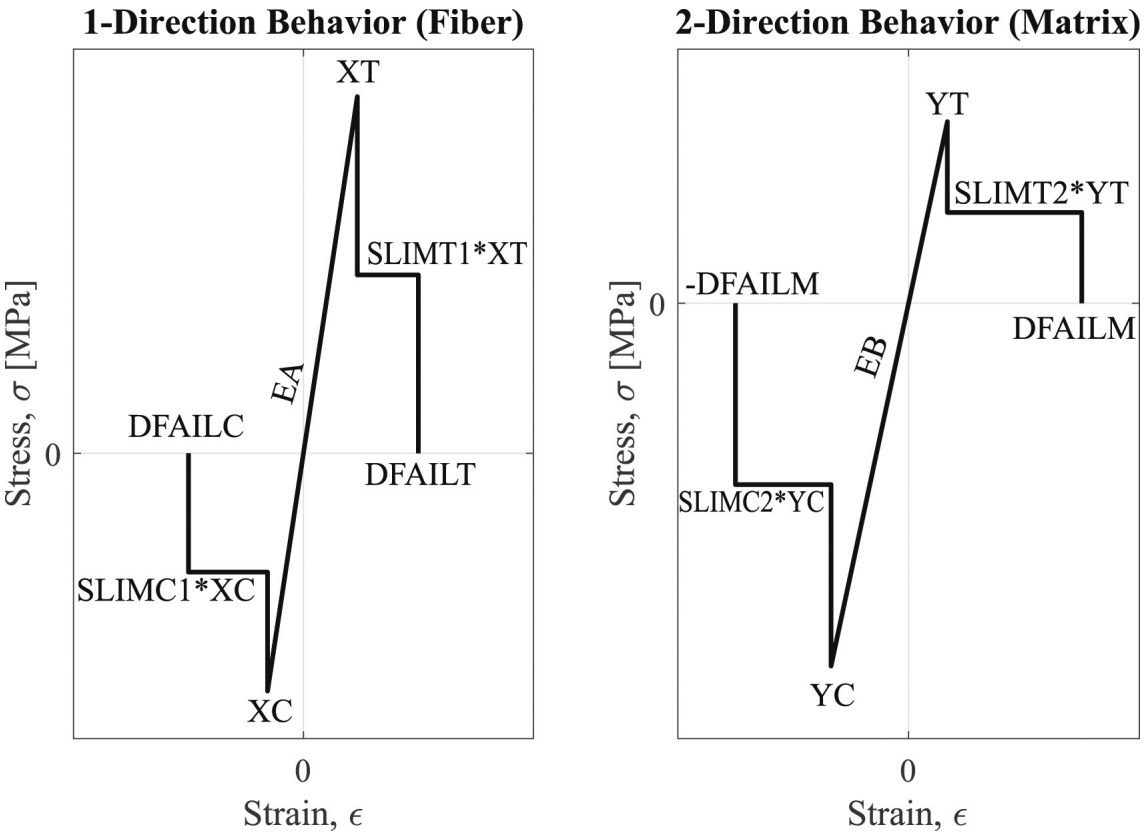

Figure 2.3: Qualitative behaviour of MAT_054 formulation.

2.4.2 MAT_026 (Honeycomb)

To represent the behaviour of the aluminium honeycomb core, the constitutive law `MAT_026 (HONEYCOMB)` was employed. As reported in the LS-DYNA documentation [14], this material formulation is specifically designed for thin-walled cellular structures and foams.

Stress–strain definition. The formulation requires the definition of stress curves that describe the average stress as a function of volumetric strain or relative volume. Figure 2.4 shows an example of stress-volumetric strain curve, where the volumetric strain is computed from the ratio between the current volume V_c and the initial volume V_0 as follows:

$$\varepsilon_v = 1 - \frac{V_c}{V_0} \tag{2.11}$$

The model automatically extrapolates the curve beyond the last tabulated points, hence the input must be defined to prevent unphysical extension into the negative strain region.

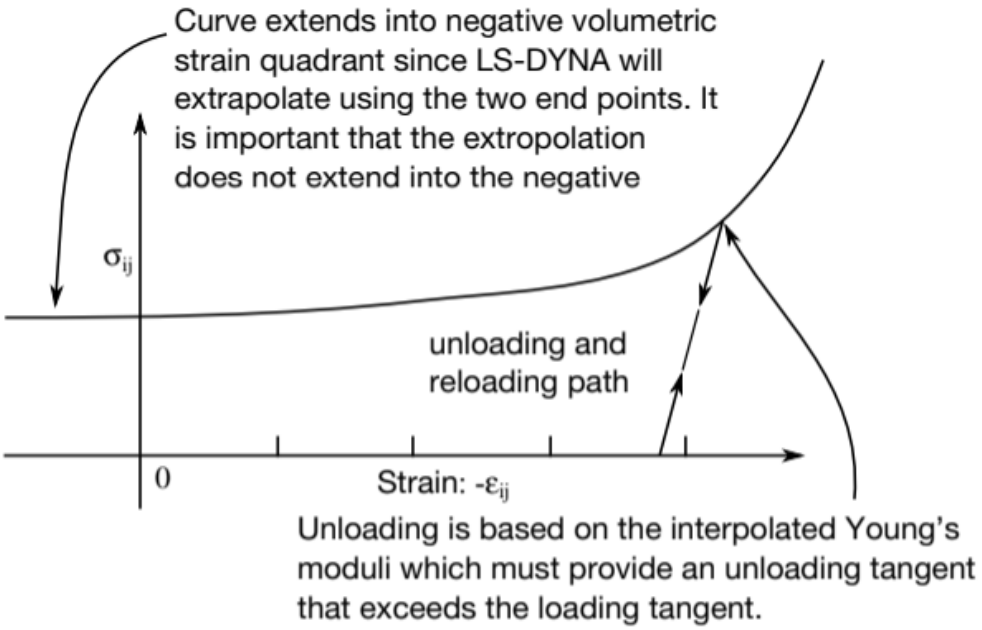

Figure 2.4: Stress-volumetric strain curve for MAT_026 formulation.

Elastic and shear moduli during compaction. Before compaction, the honeycomb core is assumed to behave as an orthotropic material with decoupled responses along normal directions. As the relative volume decreases towards the fully com-

pacted state, the elastic constants E_{aa}, E_{bb}, E_{cc} and shear moduli G_{ab}, G_{bc}, G_{ca} evolve linearly according to:

$$E_{aa} = E_{a,un} + \beta\,(E - E_{a,un}), \tag{2.12}$$
$$E_{bb} = E_{b,un} + \beta\,(E - E_{b,un}), \tag{2.13}$$
$$E_{cc} = E_{c,un} + \beta\,(E - E_{c,un}), \tag{2.14}$$
$$G_{ab} = G_{ab,un} + \beta\,(G - G_{ab,un}), \tag{2.15}$$
$$G_{bc} = G_{bc,un} + \beta\,(G - G_{bc,un}), \tag{2.16}$$
$$G_{ca} = G_{ca,un} + \beta\,(G - G_{ca,un}), \tag{2.17}$$

[14]

where $E_{x,un}, G_{x,un}$ are the initial moduli of the uncompacted honeycomb, E, G are the moduli of the fully compacted solid material, and β is defined as:

$$\beta = \max\left[\min\left(\frac{1-V}{1-V_f}, 1\right), 0\right], \tag{2.18}$$

with V the relative volume and V_f the fully compacted reference volume [14].

Stress update algorithm. At each time step, the trial stresses are updated in the local element coordinate system by adding the elastic contributions from the current strain increment:

$$\sigma_{aa}^{n+1,trial} = \sigma_{aa}^{n} + E_{aa}\,\Delta\varepsilon_{aa}, \tag{2.19}$$
$$\sigma_{bb}^{n+1,trial} = \sigma_{bb}^{n} + E_{bb}\,\Delta\varepsilon_{bb}, \tag{2.20}$$
$$\sigma_{cc}^{n+1,trial} = \sigma_{cc}^{n} + E_{cc}\,\Delta\varepsilon_{cc}, \tag{2.21}$$
$$\sigma_{ab}^{n+1,trial} = \sigma_{ab}^{n} + 2G_{ab}\,\Delta\varepsilon_{ab}, \tag{2.22}$$
$$\sigma_{bc}^{n+1,trial} = \sigma_{bc}^{n} + 2G_{bc}\,\Delta\varepsilon_{bc}, \tag{2.23}$$
$$\sigma_{ca}^{n+1,trial} = \sigma_{ca}^{n} + 2G_{ca}\,\Delta\varepsilon_{ca}. \tag{2.24}$$

[14]

These trial stresses are then compared with the tabulated stress values from the input curves; if they exceed the permissible limit, they are scaled back. For the fully compacted material, a perfectly plastic response is assumed, even in this case if the trial stress exceed the input yield stress `SIGY` it is scaled back.

Pressure update. The hydrostatic pressure component is updated at each step using the elastic bulk modulus:

$$K = \frac{E}{3(1-2\nu)}, \tag{2.25}$$

$$p^{n+1} = p^n - K\,\Delta\varepsilon_{kk}^{n+1/2}. \tag{2.26}$$

[14]

The total Cauchy stress is then recomposed as

$$\sigma_{ij}^{n+1} = s_{ij}^{n+1} - p^{n+1}\,\delta_{ij}, \tag{2.27}$$

[14]

before being transformed back into the global coordinate system.

Chapter 3

Post Analysis of the Impact Assembly with the Sandwich Anti-Intrusion Plate

As briefly outlined in the Introduction, the first design objective of this work was to reproduce the failure mechanisms observed during the crash test of the *Impact Assembly* composed by the sandwich-structured AIP and origami-designed IA. To perform post-test analyses, the AIP panel from Patruno's study [5] was remodelled in LS-DYNA with the goal of reproducing a similar failure mode.

In order to generate a representative numerical model, it was necessary to base material inputs on experimental data that mimic the load conditions experienced by the sandwich panel during impact. Specifically, the panel is subjected to an out-of-plane shear load imparted by the IA: upon impact, the attenuator deforms and fractures, absorbing a portion of the input energy and transferring the remainder to the AIP generating transverse shear stresses concentrated around the contact area and transmitted through the sandwich thickness.

3.1 Perimeter Shear Test

A comparable loading scenario is prescribed by the Formula SAE perimeter shear test described in T3.5.10 and T3.5.11 of the 2025 rulebook. Although this differs from the dynamic nature of the IA crash test, the quasi-static shear test was chosen for its resource efficiency, and relevance to the out of plane shear-driven failure mode.

The data used for the material model calibration were derived from tests previously conducted by the team on a series of laminate configurations. Specifically, the tested layups are listed in Table 3.2 where:

T Is the CFRP GG200T(T800)-DT120-42 2×2 twill-weave characterized experimentally in Chapter 2.

U Is the unidirectional high modulus CFRP prepreg HM100-24%-M46J12K with mechanical properties as in Table 3.1:

Tensile modulus (0°)	275.00	GPa
Tensile modulus (90°)	7.51	GPa
In-plane shear modulus	4.95	GPa
Tensile strength (0°)	2450	MPa
Tensile strength (90°)	44	MPa
In-plane shear strength	136	MPa

Table 3.1: Mechanical properties of HM100-24%-M46J12K.

HC Is a 20 mm thick aluminium honeycomb 1/8-5052-0.0015 6.1 pcf.

Panel	**Top Skin**	**Core**	**Bottom Skin**
P1	0T/15U/0T	HC	0T/15U/0T
P2	0T/15U/-15U	HC	-15U/15U/0T
P3	0T/45U/-45U/45U/-45U	HC	45U/-45U/45U/-45U/0T
P4	0T/0U/90U/0U/90U/0U/90U	HC	90U/0U/90U/0U/90U/0U/0T

Table 3.2: Layups of the tested sandwich panels (symmetric with Al honeycomb core).

3.1.1 Test Setup

The setup of the perimeter shear test is well defined by the Formula Student rules [2] in which the test object, fixture and load applicator are described:

- "T3.5.10: Perimeter shear tests must be completed which measure the force required to push or pull a 25 mm diameter flat punch through a flat laminate sample. The sample must be at least 100 mm × 100 mm. [...]"
- "T3.5.11: The test fixture must support the entire sample, except for a 32 mm hole aligned co-axially with the punch. The sample must not be clamped to the fixture."

The crosshead movement was imposed under displacement control at a constant rate of $4\,\mathrm{mm\,min^{-1}}$.

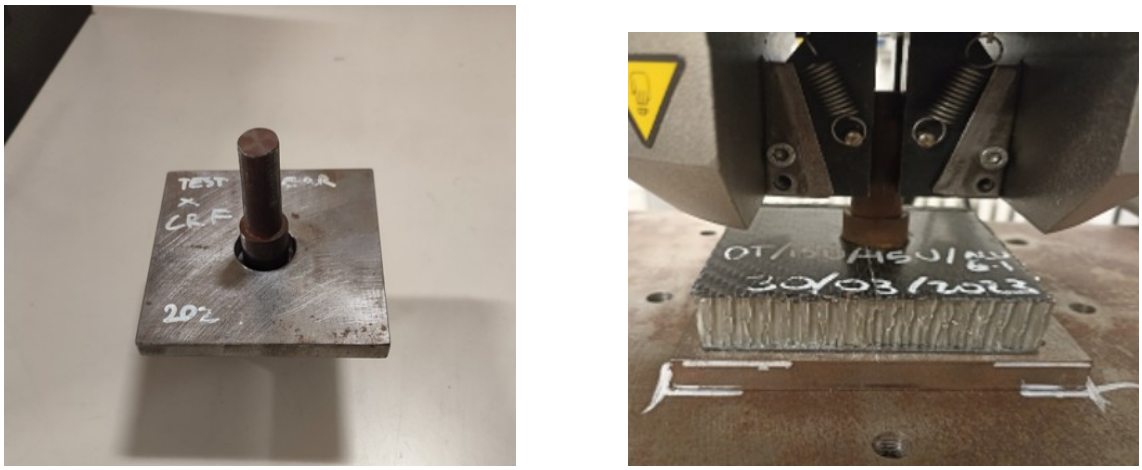

(a) (b)

Figure 3.1: Perimeter shear test configuration. (a) Fixture with dedicated punch; (b) application of the test on a sandwich panel specimen.

3.1.2 Test Results

The load-displacement curves for all panels exhibit a typical pattern: an initial elastic rise, followed by a series of local peaks caused by fibre and ply failures; then a sudden drop associated with complete top-skin failure and the onset of progressive cell-wall buckling in the underlying honeycomb. A long plateau develops as the core tears and buckles progressively; subsequently, a secondary load increase appears before the penetration of the bottom skin and finally a sharp force collapse. This sequence is qualitatively consistent with indentation studies on aluminium honeycomb cores [16]. The first peak can be interpreted as the combined effect of the skin's out-of-plane shear resistance and the onset of core buckling; the plateau follows the characteristic honeycomb force-displacement response; the second peak is lower because, at that stage, the CFRP bottom face sheet is unsupported by an intact honeycomb core and thus offers less resistance.

It should be noted that the test was conducted without applying any preload to the specimens. As a result, the initial portion of the force-displacement curve is influenced by the settling of the specimen within the fixture, rather than by the intrinsic structural response of the sandwich panel. This explains the small nonlinear deviations observed at the beginning of the experimental curves, which were therefore disregarded in the comparison with the numerical predictions.

The following charts report the force-displacement curves for each panel, while Table 3.3 indicates the plateau force evaluated as average force between 6 mm and 10 mm and the maximum force. In the 6 to 10 mm interval the contribution of the skins is absent and the response is entirely governed by core crushing.

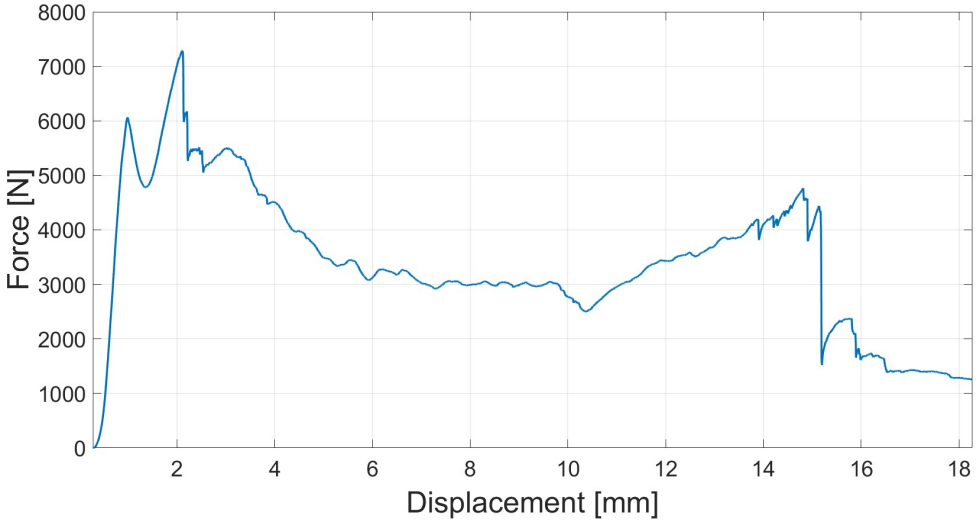

Figure 3.2: Force–displacement response from the perimeter shear test of panel P1 (layup: 0T/15U/0T).

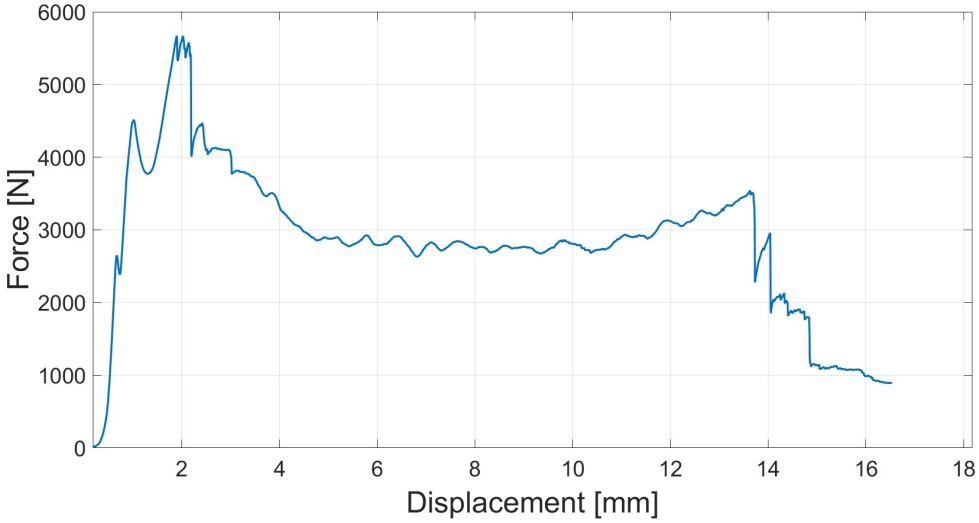

Figure 3.3: Force–displacement response from the perimeter shear test of panel P2 (layup: 0T/15U/–15U).

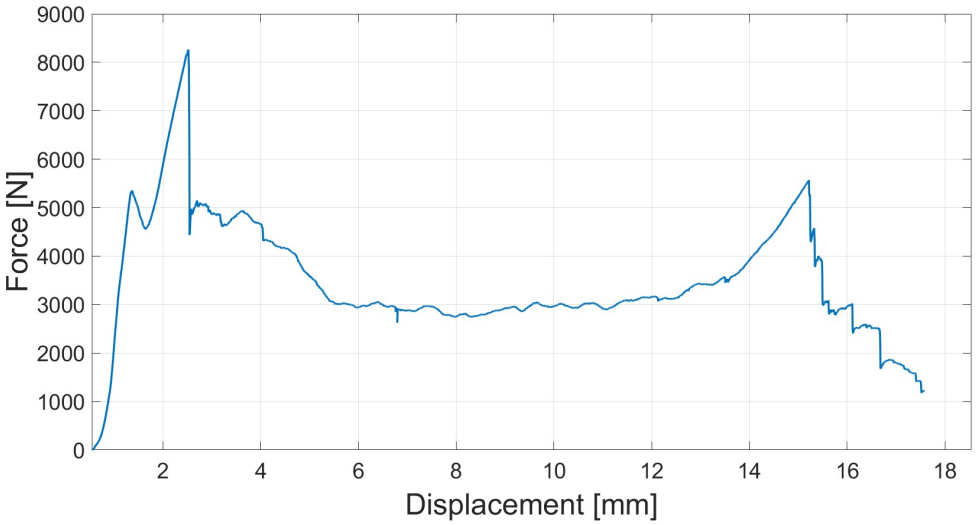

Figure 3.4: Force–displacement response from the perimeter shear test of panel P3 (layup: 0T/45U/–45U/45U/–45U).

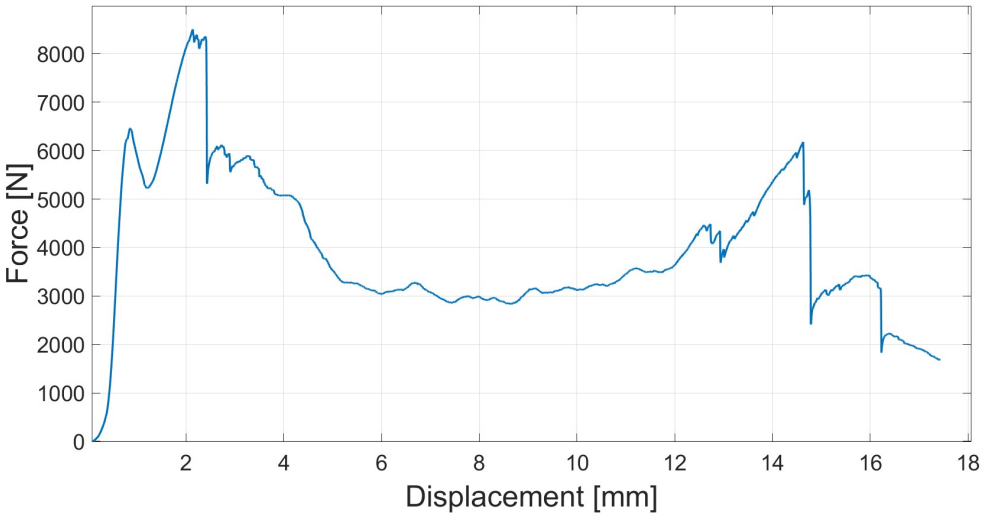

Figure 3.5: Force–displacement response from the perimeter shear test of panel P4 (layup: 0T/0U/90U/0U/90U/0U/90U).

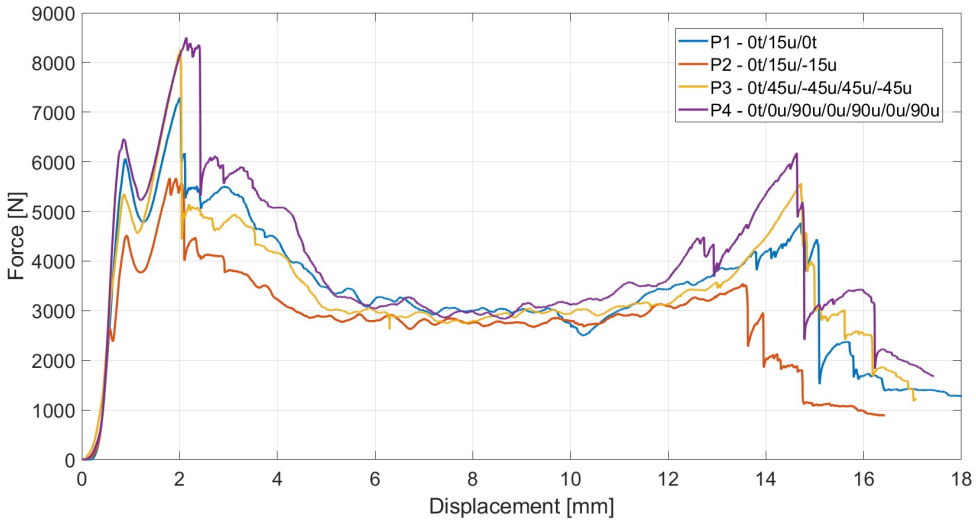

Figure 3.6: Comparative chart for force-displacement response of all panels from the perimeter shear test.

Panel	Layup	Peak Force [N]	Plateau Force [N]
P1	0T/15U/0T	7285	3048
P2	0T/15U/-15U	5671	2773
P3	0T/45U/-45U/45U/-45U	8264	2901
P4	0T/0U/90U/0U/90U/0U/90U	8503	3037

Table 3.3: Peak and plateau forces measured during perimeter shear tests for each panel.

3.2 Perimeter Shear Model

The finite element model was developed using Altair HyperMesh for mesh generation and Ansys LS-DYNA PrePost for model setup and analysis.

The simulation reproduces the perimeter shear test on a 100 mm × 100 mm sandwich panel, adopting a reduced quarter-symmetry model for both the panel and the flat cylindrical punch (25 mm diameter), in order to minimise computational cost (see Figure 3.7). The fixture described in Section 3.1.1 was modelled by constraining the bottom nodes of the panel while introducing a 32 mm diameter cutout.

The numerical analysis was focused on reproducing only the first half of the experimental load-displacement curve. This interval captures two key failure mechanisms:

- The fracture of the loaded face sheet;
- The onset of core compaction directly under the punch.

Extending the simulation to the full crushing plateau would have implied a considerable increase in computational cost without providing additional information relevant to the activation of the failure. Therefore, restricting the model to the initial part of the response was considered a good compromise: It ensures that the correct collapse is triggered when the AIP model is integrated into the complete *Impact Assembly*, while avoiding unnecessary computational burden. This strategy was sufficient for the purpose of assessing system-level crashworthiness.

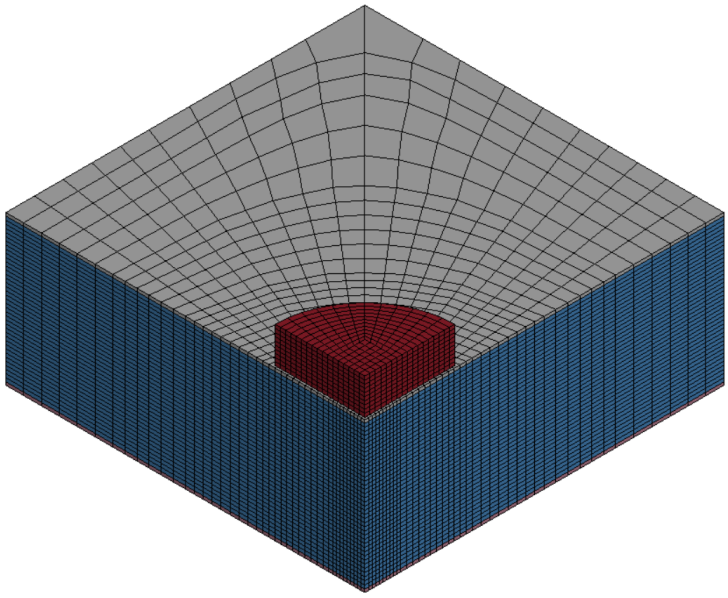

Figure 3.7: FEM model of the perimeter shear test, showing the quarter reduced sandwich specimen and punch.

3.2.1 Model Setup

Mesh generation strategy

To accurately capture the localized stress distribution near the punch area, a tailored 2D radial mesh was created in HyperMesh. A 50 mm × 50 mm surface was first generated in CATIA, with reference lines sketched to guide the mesh partitioning (Figure 3.8a). Surface and sketches were then imported into HyperMesh to define separate meshing regions, enabling fine element sizing near the punch area and progressively coarser elements towards the panel edges (Figure 3.8b).

The mesh was refined and optimised using HyperMesh quality tools, achieving a computed `Quality Index` (QI) of 0.06 after excluding the `Min Size` parameter, irrelevant to the adopted gradation strategy.

The completed 2D mesh was exported to LS-DYNA, where the full 3D panel geometry was obtained by duplicating the shell mesh to obtain the two CFRP skins

and extruding it into solid elements representing the honeycomb core. The upper and lower CFRP skins were modelled as shell elements directly associated with composite layups by using the `PART_COMPOSITE` option. The punch was generated within LS-PrePost using the `Shape Mesher` tool and subsequently reduced to a quarter section through element deletion.

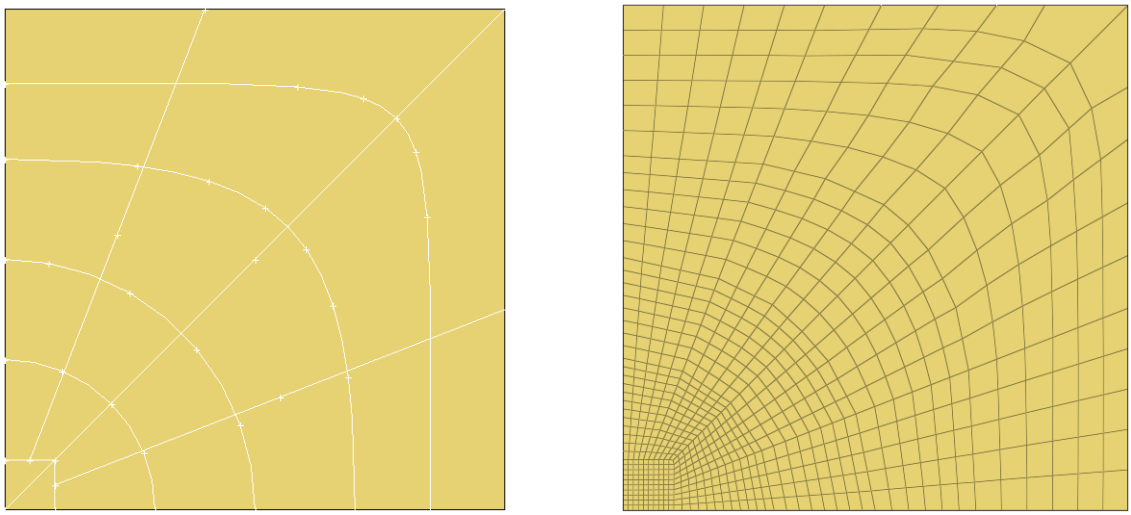

(a) (b)

Figure 3.8: Creation of the 2D mesh for the perimeter shear model. (a) Quarter panel with reference lines imported from the .stp geometry to guide the mesh generation; (b) resulting mesh exported to LS-DYNA.

Element formulation

The honeycomb core was meshed with solid bricks using `ELFORM = -2`, a fully integrated, selective-reduced (S/R) 8-node formulation. [17].

The punch was defined with the default solid formulation `ELFORM = 1`; since it is assigned `MAT_020_RIGID`, it behaves as a rigid body and the choice of solid integration has negligible influence on the solution.

The CFRP skins were discretised with shell elements using `ELFORM = 16`, a fully integrated shell formulation . In addition, the shear correction factor `SHRF` in the `PART_COMPOSITE` cards was set to 0.83333, as recommended by the LS-DYNA manual[17].

Contact definition

`CONTACT_AUTOMATIC_SURFACE_TO_SURFACE` was defined between the punch and the top skin and between the punch and the core introducing static and dynamic coefficient of friction respectively 0.2 and 0.15 in values. The skins and the core

were modelled as a single continuum by merging coincident nodes at the interfaces. This modelling choice is motivated by the experimental evidence from the conducted tests: the dominant failure mechanisms under perimeter shear loading are fibre–matrix fracture in the CFRP skins and local buckling and tearing of the aluminium honeycomb directly beneath the punch footprint, whereas interfacial delamination is secondary. To keep the model simple and focused on the governing mechanisms, delamination was therefore neglected.

Boundary conditions

The panel was clamped by constraining the bottom nodes in all six degrees of freedom (three translational and three rotational). A circular cutout of 32 mm in diameter was introduced to reproduce the central opening of the experimental fixture, with the corresponding nodes free of constraints to reproduce the experimental boundary conditions. Since the model exploits quarter symmetry, only a quarter of the hole is actually present in the finite element model, located at the corner of the panel domain.

The model reduction was achieved by imposing symmetry boundary conditions on the lateral faces of the 50 mm × 50 mm quarter panel.

Loading was applied through the punch by prescribing a linear time–displacement curve along the vertical axis, while all the remaining degrees of freedom were constrained directly by means of the `MAT_020_RIGID` options.

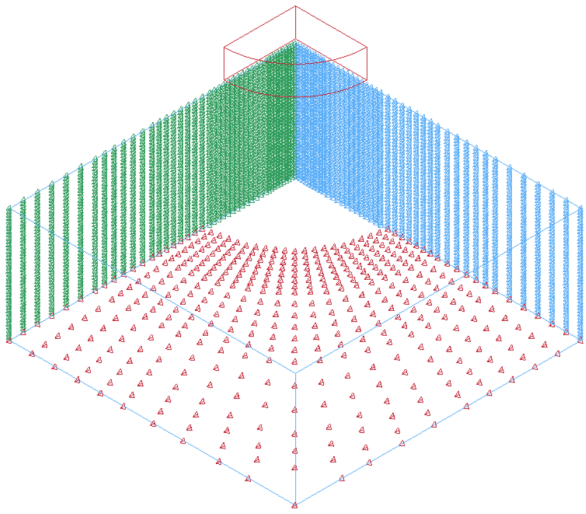

Figure 3.9: Boundary conditions of the perimeter shear panel: fixed bottom nodes simulating the fixture with 32 mm cutout (red), and symmetry constraints applied to the lateral faces (green and blue).

To reduce the computational cost, the punch speed was set significantly higher than the experimental cross-head rate, while preserving the realism of the structural response as shown by the simulation results.

3.2.2 Material Cards

The numerical model relies on three different material formulations:

- `MAT_054_ENHANCED_COMPOSITE_DAMAGE` for the CFRP skins;
- `MAT_026_HONEYCOMB` for the aluminium honeycomb core;
- `MAT_020_RIGID` for the punch.

The detailed input parameters for each card are discussed in the following.

Since LS-DYNA does not explicitly define unit systems, it is crucial to adopt a consistent convention for all input data. In this model, the coherent unit system is defined by:

- Mass = g;
- Length = mm;
- Time = ms.

From these base units, the derived quantities are force in N, stress in MPa, energy in mJ, and density in $\mathrm{g\,mm^{-3}}$.

CFRP

The material input parameters for the two prepreg systems investigated in this work are summarized in Table 3.4 and Table 3.5, respectively.

From the analysis of the tables, it emerges that the stiffness parameters did not require any calibration with respect to datasheet values or test data. Conversely, an accurate calibration of the failure stresses was necessary to achieve agreement between experimental and numerical results. The tuning process started from the values obtained by the characterisation tests (T800 prepreg tensile and shear parameters) or datasheets (M46J prepreg parameters and T800 compression data).This task was further complicated by the desire to ensure the predictive capability of the model, which required identifying a set of parameters able to guarantee the transferability of the material cards across different configurations. Another critical aspect concerned the tuning of the parameters reported in rows 4 and 5 of the tables. Their

calibration was guided by the work of Wade et al. [8], which provides a useful reference for their definition. Starting from these guidelines, the values reported here were obtained through a trial and error procedure.

An important advantage of this modelling strategy is that, once an adequate set of parameters has been identified, it is possible to reproduce the behaviour of different laminates by keeping a consistent material card and simply adjusting the number and orientation of the plies in the `PART_COMPOSITE` definition. This feature enables the prediction of the structural response of a wide range of stacking sequences without requiring a full revision of the material parameters for each case, thus ensuring both accuracy and efficiency in the simulations.

	RO $1.7e-3$	**EA** $2.75e+5$	**EB** 7 510	**(EC)**	**PRBA**	**(PRCA)**	**(PRCB)**
GAB 4 950	**GBC** 4 950	**GCA** 4 950	**(KF)**	**AOPT** 2.0	**2WAY** 1.0		
XP	**YP**	**ZP**	**A1** 1.0	**A2** 0.0	**A3** 0.0	**MANGLE**	
V1	**V2**	**V3**	**D1**	**D2**	**D3**	**DFAILM** 0.0267	**DFAILS** 0.0275
TFAIL 0.0	**ALPH** 0.0	**SOFT** 0.35	**FBRT** 1.0	**YCFAC** 1.0	**DFAILT** 0.089	**DFAILC** −0.0043	**EFS**
XC −950	**XT** 1 960	**YC** −160	**YT** 35	**SC** 109	**CRIT** 54	**BETA** 0.0	
PEL	**EPSF**	**EPSR**	**TSMD**	**SOFT2** 1.0			
SLIMT1 0.1	**SLIMC1** 0.1	**SLIMT2** 0.1	**SLIMC2** 0.1	**SLIMS** 0.5	**NCYRED**	**SOFTG** 1.0	
LCCX	**LCXT**	**LCYC**	**LCYT**	**LCSC**	**DT**		

Table 3.4: MAT_054 HM100-24%-M46J12K input data.

	RO $1.5e-3$	**EA** $6.280e+4$	**EB** $6.280e+4$	**(EC)**	**PRBA**	**(PRCA)**	**(PRCB)**
GAB 2 960	**GBC** 2 960	**GCA** 2 960	**(KF)**	**AOPT** 2.0	**2WAY** 1.0		
XP	**YP**	**ZP**	**A1** 1.0	**A2** 0.0	**A3** 0.0	**MANGLE**	
V1	**V2**	**V3**	**D1**	**D2**	**D3**	**DFAILM** 0.00928	**DFAILS** 0.044
TFAIL 0.0	**ALPH** 0.0	**SOFT** 0.35	**FBRT** 1.0	**YCFAC** 1.0	**DFAILT** 0.0906	**DFAILC** −0.00928	**EFS**
XC −642	**XT** 626	**YC** −642	**YT** 626	**SC** 142	**CRIT** 54	**BETA** 0.0	
PEL	**EPSF**	**EPSR**	**TSMD**	**SOFT2** 1.0			
SLIMT1 0.1	**SLIMC1** 0.1	**SLIMT2** 0.1	**SLIMC2** 0.1	**SLIMS** 0.5	**NCYRED**	**SOFTG** 1.0	
LCCX	**LCXT**	**LCYC**	**LCYT**	**LCSC**	**DT**		

Table 3.5: MAT_054 GG200T(T800)-DT120-42 input data.

Honeycomb

The core was modelled using the `MAT_026_HONEYCOMB` formulation, calibrated to reproduce the characteristic plateau stress observed in the experimental perimeter shear test. The detailed input parameters for the material card are reported in Table 3.6.

The densification curve, used as input for the stress-volumetric strain curve identified in the card by the `LCA` tab, was derived from the experimental crush behaviour reported by Ciepielewski and Miedzińska [18]. In particular, Figure 9 (page 7) in that work was used as a reference for the plateau and post-buckling stages, which were then adapted to match the honeycomb experimental characteristics in this study.

Following the recommendations provided in the LS-DYNA material manual [14], the initial linear elastic region up to the onset of cell buckling was omitted, and only the plateau and densification stages were retained. The resulting curve is presented in Figure 3.10. This approach was found to reduce numerical oscillations in the force response during the compaction of the solid core elements, improving the overall stability and accuracy of the simulation results.

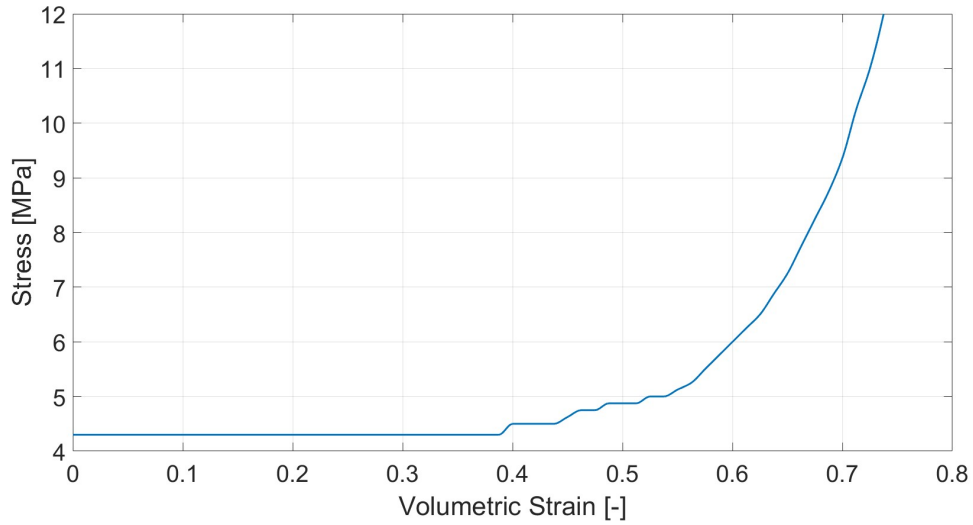

Figure 3.10: Honeycomb Stress - Volumetric strain curve, used to define the LCA input for MAT_026.

	RO	**E**	**PR**	**SIGY**	**VF**	**MU**	**BULK**
	$9.77e-5$	$7.10e+4$	0.33	152	0.2435	0.05	
LCA	**LCB**	**LCC**	**LCS**	**LCAB**	**LCBC**	**LCCA**	**LCSR**
2							
EAAU	**EBBU**	**ECCU**	**GABU**	**GBCU**	**GCAU**	**AOPT**	**MACF**
1862			10	20	20	2	1
XP	**YP**	**ZP**	**A1**	**A2**	**A3**		
			0.0	0.0	1.0		
D1	**D2**	**D3**	**TSEF**	**SSEF**	**V1**	**V2**	**V3**
1.0	0.0	0.0	0.4	0			

Table 3.6: MAT_026 input data.

3.2.3 Simulation Results and Solver Settings

The simulations were performed using the LS-DYNA explicit solver. Time step control was applied through `DT2MS` parameter.

In explicit finite element solvers, the stable time step is limited by the smallest element characteristic length and by the local wave propagation speed. To accelerate the simulation without modifying the mesh or material stiffness, mass scaling can be applied. This technique artificially increases the element density and hence its inertia to achieve a larger time increment.

Automatic mass scaling in LS-DYNA is controlled by the parameter `DT2MS` in the card `CONTROL_TIMESTEP`. When `DT2MS` is assigned a negative value, additional mass is applied only to those elements whose natural time step would fall below `|DT2MS|`. Their density is locally increased so that their new stable time step equals `|DT2MS|`, leaving the rest of the mesh unaffected.

Conversely, specifying a positive `DT2MS` forces all elements to share the same time step, either by adding or removing mass across the mesh.

In this work, a target time step of `DT2MS` $= -5.0 \times 10^{-4}$ was adopted, leading to a substantial artificial mass increase up to approximately 450 times the actual physical mass. Although such a large scaling factor is non-physical, it was required to obtain computationally feasible runtimes. The numerical results were not significantly affected, as the deviation from the experimental forces remained below 10% for all panels, with the only exception being the plateau force of panel P2.

The analysis focusses on the ability of the model to reproduce the load increase up to the top skin failure and the subsequent plateau force. Table 3.7 reports the numerical maximum and plateau forces, together with the corresponding errors with respect to the experimental values. The charts, on the other hand, allow for a qualitative assessment of the strengths and limitations of the numerical models, highlighting both the accuracy in capturing the overall trends and the discrepancies in reproducing local features of the response.

The comparison between experimental and numerical curves shows that the elastic region and the deviation from linearity are well captured by the model, as well as the maximum load and the plateau force. These features indicate that the progressive damage of the face sheet and the compaction of the core are reproduced with sufficient accuracy.

The simulation is less accurate in modelling the first fracture event, characterised in the experiments by a partial load drop followed by a recovery. This behaviour is not correctly reproduced by the simulations. Secondly, the experimental curves exhibit a sudden load drop in correspondence of the top skin failure followed by

a smoother load decrease likely associated with the fraying of the residual fibres. The simulation tend to predict a sudden collapse directly towards the plateau stress level. An exception is represented by the P2 laminate, where the model shows a more gradual reduction in load, closer to the experimental trend, but then the plateau force is not correctly calculated. In all other laminates, the transition from peak to plateau is predicted in a more abrupt manner.

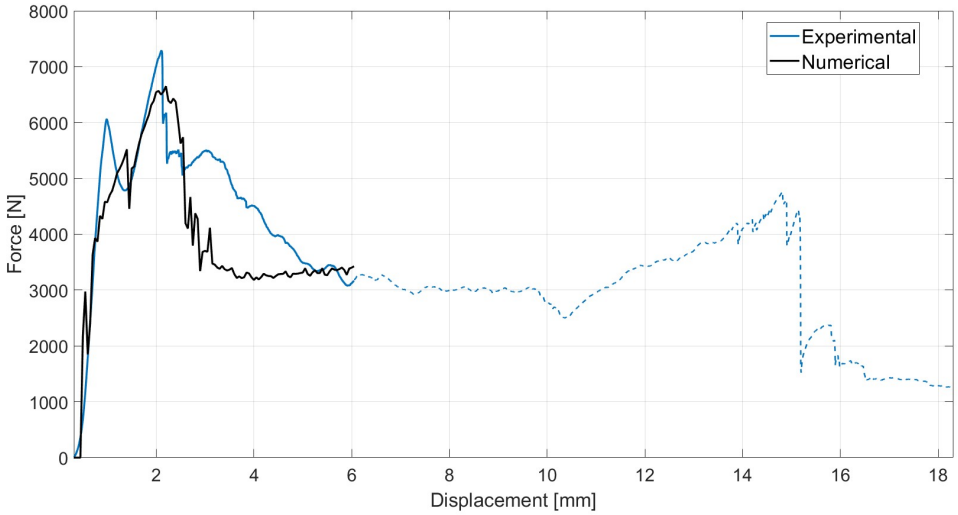

Figure 3.11: Force-displacement response of panel P1 (layup: 0T/15U/0T): comparison between experimental perimeter shear test and numerical model.

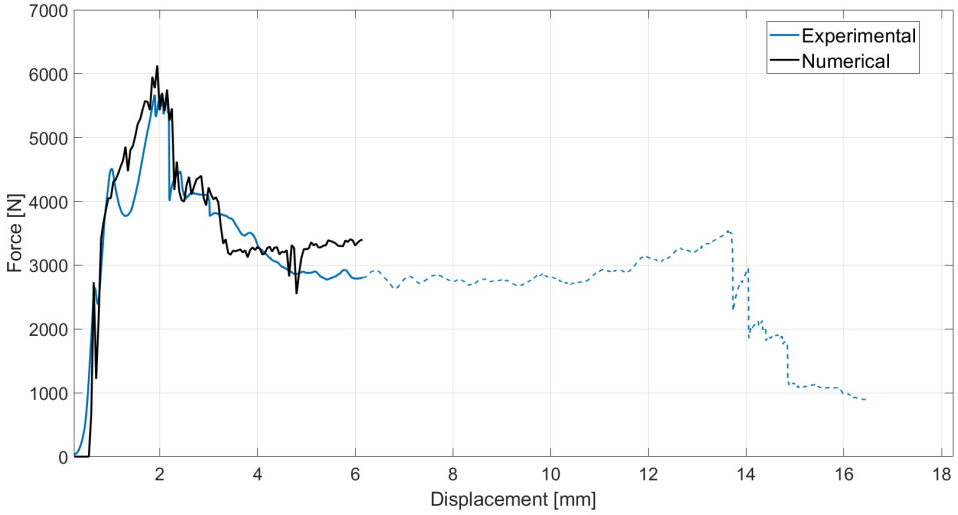

Figure 3.12: Force-displacement response of panel P2 (layup: 0T/15U/–15U): comparison between experimental perimeter shear test and numerical model.

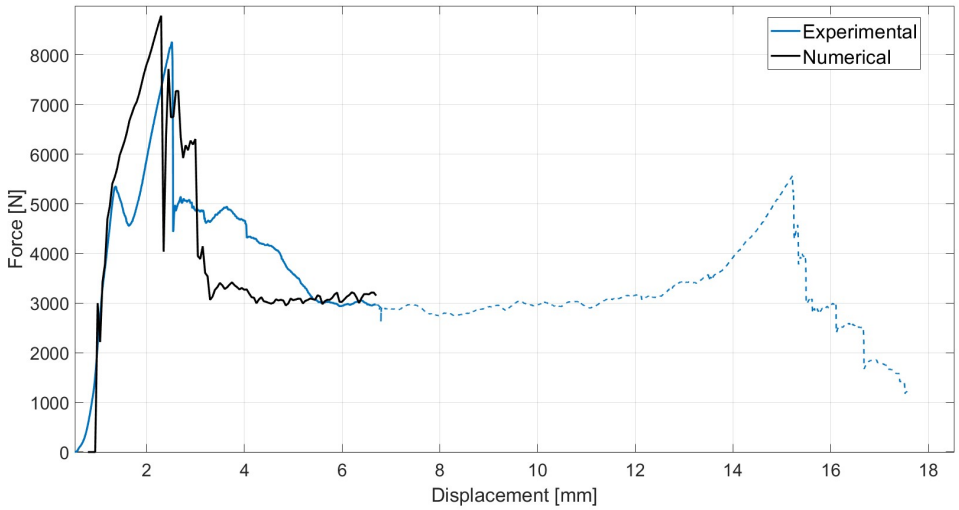

Figure 3.13: Force-displacement response of panel P3 (layup: 0T/45U/–45U/45U/–45U): comparison between experimental perimeter shear test and numerical model.

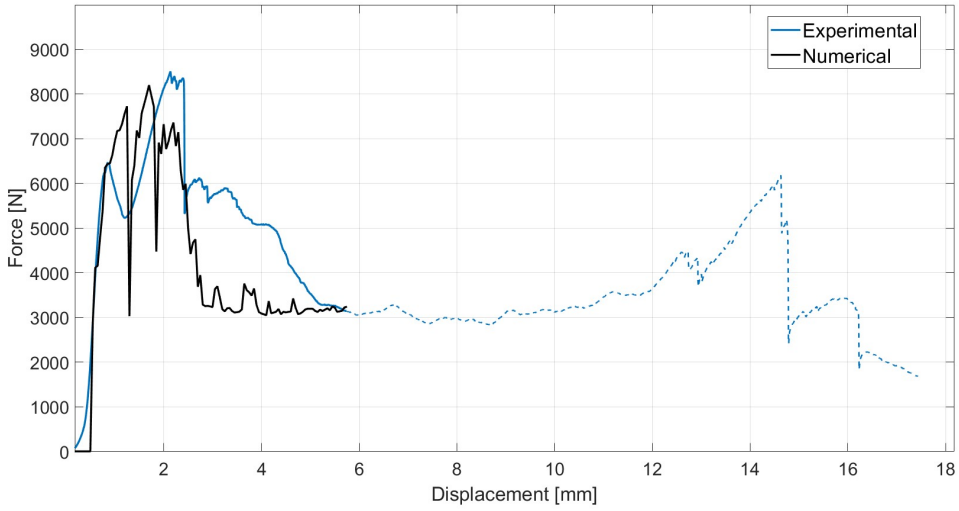

Figure 3.14: Force-displacement response of panel P4 (layup: 0T/0U/90U/0U/90U/0U/90U): comparison between experimental perimeter shear test and numerical model.

Panel	$F_{\mathbf{max,num}}$ [N]	$\mathbf{err}F_{\mathbf{max,num}}$ [%]	$F_{\mathbf{plateau,num}}$ [N]	$\mathbf{err}F_{\mathbf{plateau,num}}$ [%]
P1	6651	-8.7	3309	8.6
P2	6128	8.1	3255	17.4
P3	8789	6.4	3097	6.8
P4	8195	-3.6	3171	4.4

Table 3.7: Comparison between experimental and numerical results: simulated peak and plateau forces with relative errors.

3.3 Integrated Sandwich Impact Assembly Model

The results obtained from the perimeter shear model were used to develop a new sandwich AIP model, based on the layup configuration reported in the State of the Art (Section 1.2.3), specifically 0T/0U/90U/45U/-45U/0U/90U with an aluminium honeycomb core 1/8-5052-0.0015, 6.1 pcf. This AIP model was integrated with the IA model developed by Patruno [5] to obtain the complete *Impact Assembly*.

3.3.1 Model Setup

For the AIP, the material cards calibrated in Section 3.2 were adopted, while the IA model was kept identical to the validated configuration reported in Patruno's work.

Since Patruno's model employed the kg, mm, ms system of units, the data of the material cards derived from the perimeter shear model were rescaled accordingly.

A schematic overview of the integrated model is shown in Figure 3.15.

The model reduction is obtained by exploiting symmetry with respect to the horizontal mid-plane; further simplifications were avoided since they would have altered the actual boundary conditions of the IA and led to an artificially stiff response.

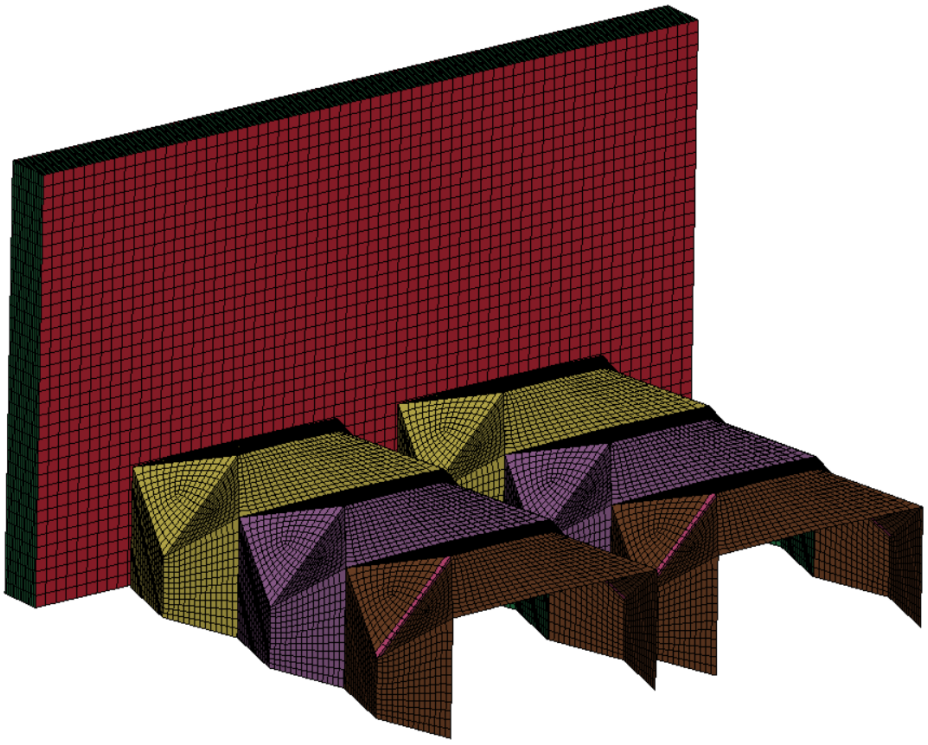

Figure 3.15: Integrated FEM model of the IA from Patruno combined with the sandwich AIP derived from the perimeter shear simulations.

Boundary conditions

Boundary conditions were defined according to the *Squadra Corse* 2024 bulkhead opening, fully constraining the nodes of the bolted interface in all six degrees of freedom (see Figure 3.16).

The loading scenario reproduced the FORMULA SAE requirement T3.18.1, which specifies an impact mass of 300 kg and an impact velocity of $7\,\mathrm{m\,s^{-1}}$ [2]. In the reduced model, symmetry was taken into account by applying half of the prescribed mass (150 kg). A `RIGIDWALL_PLANAR_MOVING` was defined accordingly to represent the impact barrier.

Contact definition

The interaction between components was modelled in two steps. The initial bonding between the IA and the AIP skins was reproduced using `CONTACT_TIED_NODE_TO_SURFACE_OFFSET`, applied to the bottom nodes of the IA and the top skin of the AIP. In addition, a `CONTACT_AUTOMATIC_SURFACE_TO_SURFACE` was defined between the AIP and the `SET_PART_LIST` of the IA shell modules to simulate the progressive interaction during the crushing phase. Static and dynamic friction coefficients of 0.2 and 0.1, respectively, were assigned to this contact card.

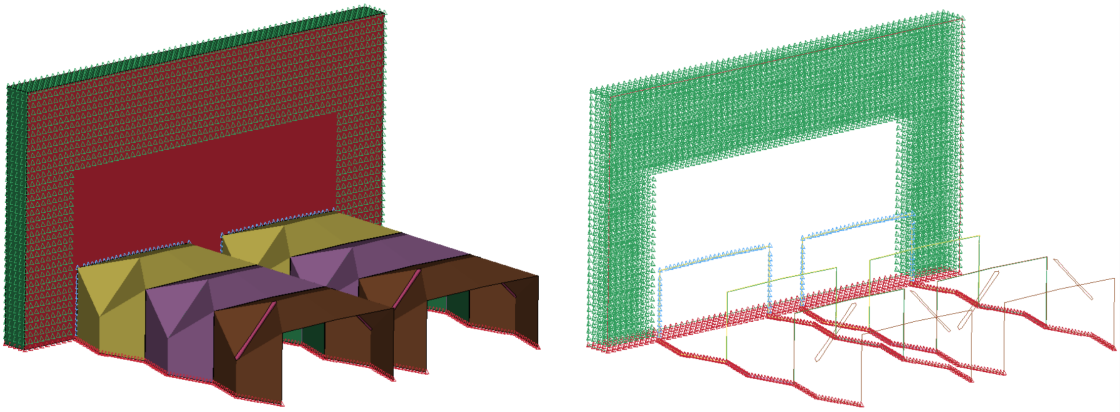

Figure 3.16: Visualization of the SPCs applied in the integrated model: bonding with the bulkhead (green), symmetry constraints (red), and bonding between AIP and IA (blue).

3.3.2 Simulation Results and Solver Settings

The simulations were performed using the LS-DYNA explicit solver. The energy balance included both hourglass and dissipation energies. To mitigate hourglass modes in the CFRP skins, hourglass control type 8 was adopted, which activates the full projection warping stiffness for shell formulations 16 and -16.

The response of the AIP was evaluated by analysing both the maximum principal stress on the average surface of the top skin and the failure indicators associated with the `MAT_054` material card. A generalized failure of the upper skin elements was observed around 22 ms, as evidenced by the behaviour of variable 5 (total failure flag) in the `MAT_054` output, which switched to 0 for most elements in the contact region, indicating complete element deletion.

The stress evolution exhibited three distinct peaks. The first occurred at approximately 11 ms, reaching about 355 MPa (Figure 3.17a) and was confined to a limited group of elements that were subsequently deleted (Figure 3.17b). The second peak, reaching 500 MPa, coincided with the generalized failure event at 22 ms (Figure 3.17c), when the ring of elements directly beneath the IA started to fail. Finally, a third peak of approximately 680 MPa was recorded during the rebound phase, as the rigid wall—having not been fully stopped—impacted the AIP again (Figure 3.17d).

A comparison between the crash test and the numerical simulation highlights that the failure load of the upper skin was approximately 57 kN in the experiment and 51 kN in the simulation, corresponding to an underestimation of about 11%.

Overall, the simulation properly reproduced the failure observed during the crash

test, confirming that a more refined AIP model would be capable of predicting the experimental behaviour.

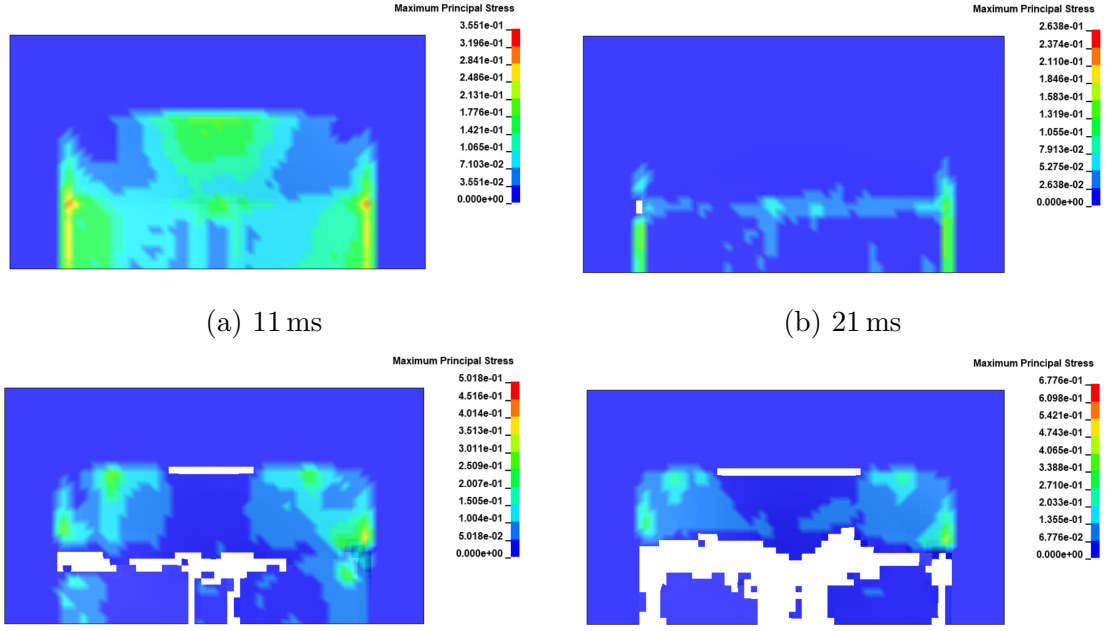

(a) 11 ms (b) 21 ms

(c) 22 ms (d) 34 ms

Figure 3.17: Heat map showing the stress state of the AIP top skin at different time-steps.

Chapter 4

Development of the Monolithic Anti-Intrusion Plate

The analysis conducted in Chapter 3 successfully reproduced the failure scenario observed during the crash test of the sandwich AIP *Impact Assembly*, thus confirming the initial hypothesis and demonstrating the inadequacy of this design for the intended application. To improve the performance of the *Impact Assembly*, two main alternatives were identified:

- Enlargement of the contact area between the components;
- Improvement of the mechanical performance of the AIP under out-of-plane shear loading.

The first alternative would require a complete redesign of the entire system. The extension of the contact area between the two components is not compatible with the use of a CFRP shell IA, such as the one designed by Patruno or those developed by other teams.

The second approach is simpler from a conceptual, engineering, and manufacturing perspective. To enhance the out-of-plane performance of the AIP, the primary objective is to increase the cross-sectional area that resists shear loading. Achieving this requires the removal of the weakest structural element. As demonstrated by the experimental studies reported in Section 3.1, the honeycomb core provides the least resistance to penetration during the perimeter shear test. Therefore, it is expected to be more effective to replace the core with additional plies of CFRP.

The objective of this chapter is to evaluate the effectiveness of a monolithic AIP solution, applying the same methodology used in Chapter 3. The optimal outcome would be a rule-compliant AIP capable of passing the required crash test while

ensuring further weight savings compared to the previous design variants developed by *Squadra Corse Polito*.

4.1 Drop Weight Impact Test

The first stage of the new design proposal consisted in acquiring experimental data to serve as a basis for the calibration of the numerical model and the tuning of the material cards.

The experimental campaign was carried out following the ASTM D7136 standard for impact testing of composite laminates [19]. A total of nine square specimens (100 mm × 100 mm) were tested, divided into three groups with nominal thicknesses of 2 mm (specimens 1-3), 4 mm (specimens 4-6) , and 6 mm (specimens 7-9) (see Figure 4.1). The material selected for the monolithic plate is the T800 prepreg characterised in Chapter 2 and indicated with the letter T in Table 4.1 where the details of the specimens are reported.

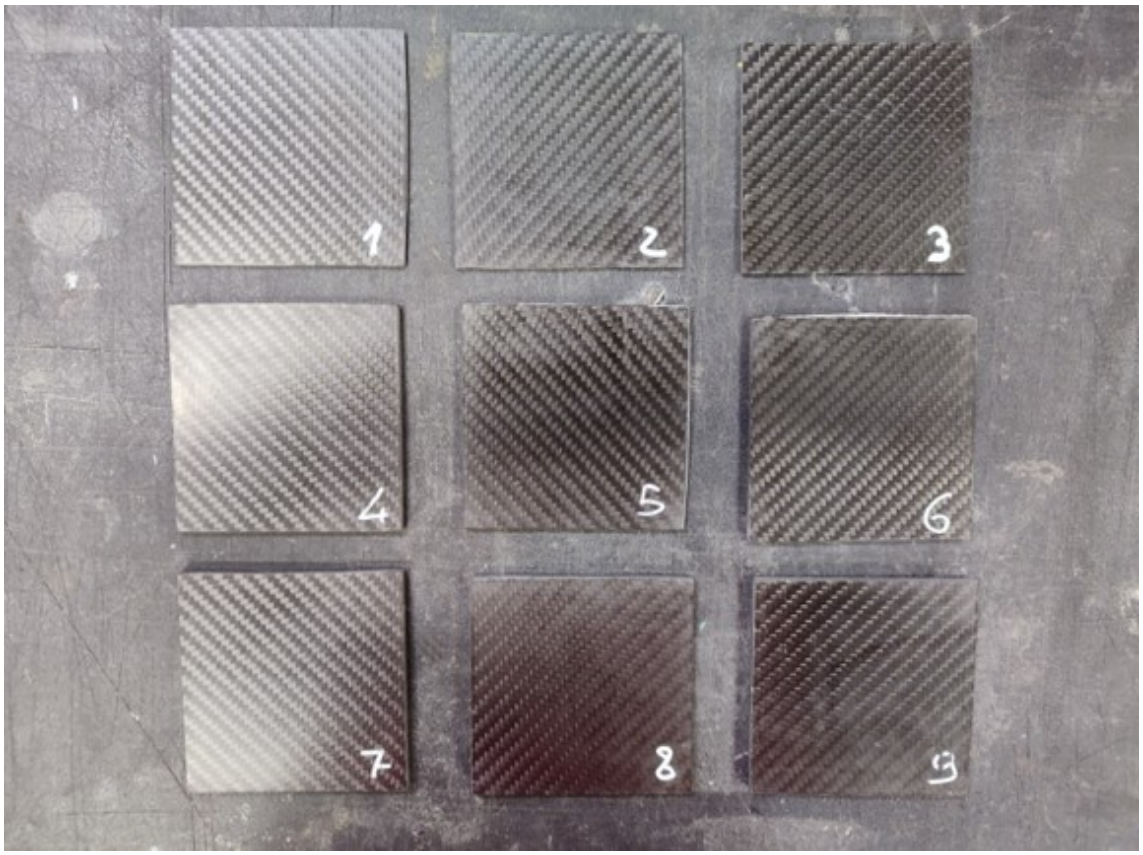

Figure 4.1: Drop weight impact test specimens.

Specimen	Layup	Nominal thickness [mm]	Measured thickness [mm]
D1	$[0T]_9$	2.00	1.89
D2			1.99
D3			1.90
D4	$[0T]_{18}$	4.00	4.01
D5			3.98
D6			3.85
D7	$[0T]_{26}$	6.00	5.91
D8			5.87
D9			5.86

Table 4.1: Drop weight impact test specimens specifications.

4.1.1 Specimens Production

The specimens were manufactured by hand lay-up on a pre-released steel plate. For each nominal thickness, rectangular laminates with dimensions of 100 mm × 300 mm were produced. The laminates were covered with additional pre-released steel plates in order to ensure uniform pressure distribution during curing and to obtain a good surface finish. The laminates were then vacuum bagged and cured in an autoclave under a pressure of 4 bar at a temperature of 130 °C for a duration of 90 min. After curing, the panels were cut into individual test specimens using a band saw.

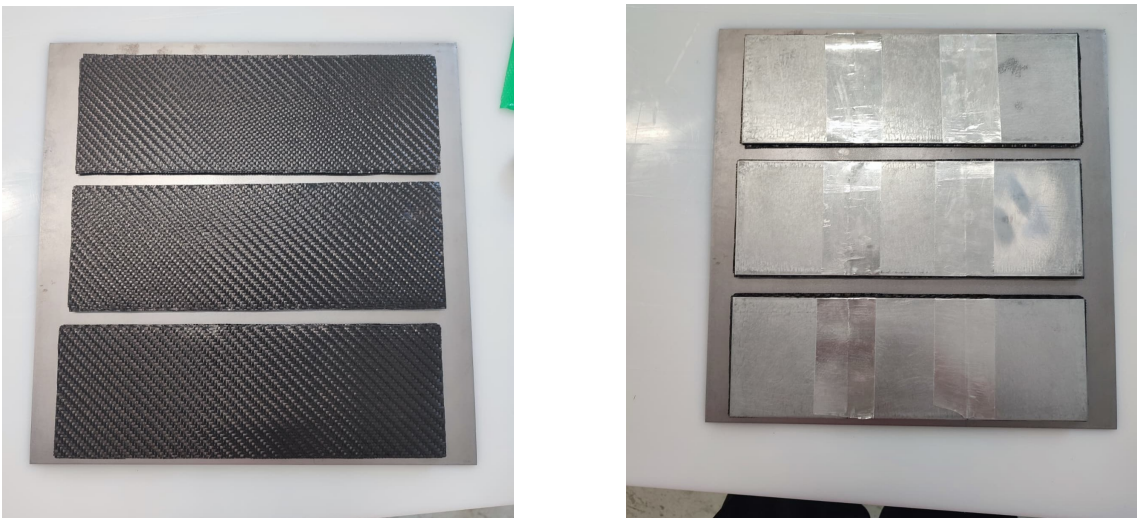

(a) (b)

Figure 4.2: Drop weight impact specimens lamination process.

4.1.2 Test Setup

The experimental campaign was carried out using an *Instron Fractovis* drop dart machine. The machine is equipped with a load cell that directly records the force history during impact.

The specimens were positioned at the center of the support fixture by means of alignment pins, and then hydraulically clamped to avoid any undesired movement or bouncing during the test. The fixture consisted of a frame with a circular cutout of 76 mm in diameter in correspondence with the impact area. The impactor was a cylindrical dart equipped with a hemispherical head of 20 mm in diameter (see Figure 4.3).

The impact velocity was set to $7\,\mathrm{m\,s^{-1}}$ in order to reproduce, as closely as possible, the dynamic conditions of the FORMULA SAE crash test. This choice ensures a representative material response in terms of strain rate dependent behaviour. The impact mass was instead adjusted according to the specimen thickness, with the objective of achieving full penetration of the dart and so exploiting the complete energy absorption capability of each configuration.

Prior to the execution of the full test campaign, a preliminary trial was conducted on one of the 2 mm specimens, used as a sacrificial sample. This step was necessary to verify the feasibility of the selected boundary conditions and to calibrate the test parameters (velocity and mass) in practice. Based on the result of this preliminary test and the operator's experience, the definitive test matrix reported in Table 4.2 was established where the specimen D1 is the sacrificial one.

Specimen	**Initial speed [m/s]**	**Impact mass [kg]**	**Impact energy [J]**
D1	4.0	5.5	44.0
D2	7.0	5.5	134.8
D3	7.0	5.5	134.8
D4	7.0	5.5	134.8
D5	7.0	5.5	134.8
D6	7.0	5.5	134.8
D7	7.0	10.5	257.3
D8	7.0	10.5	257.3
D9	7.0	10.5	257.3

Table 4.2: Drop weight impact test matrix.

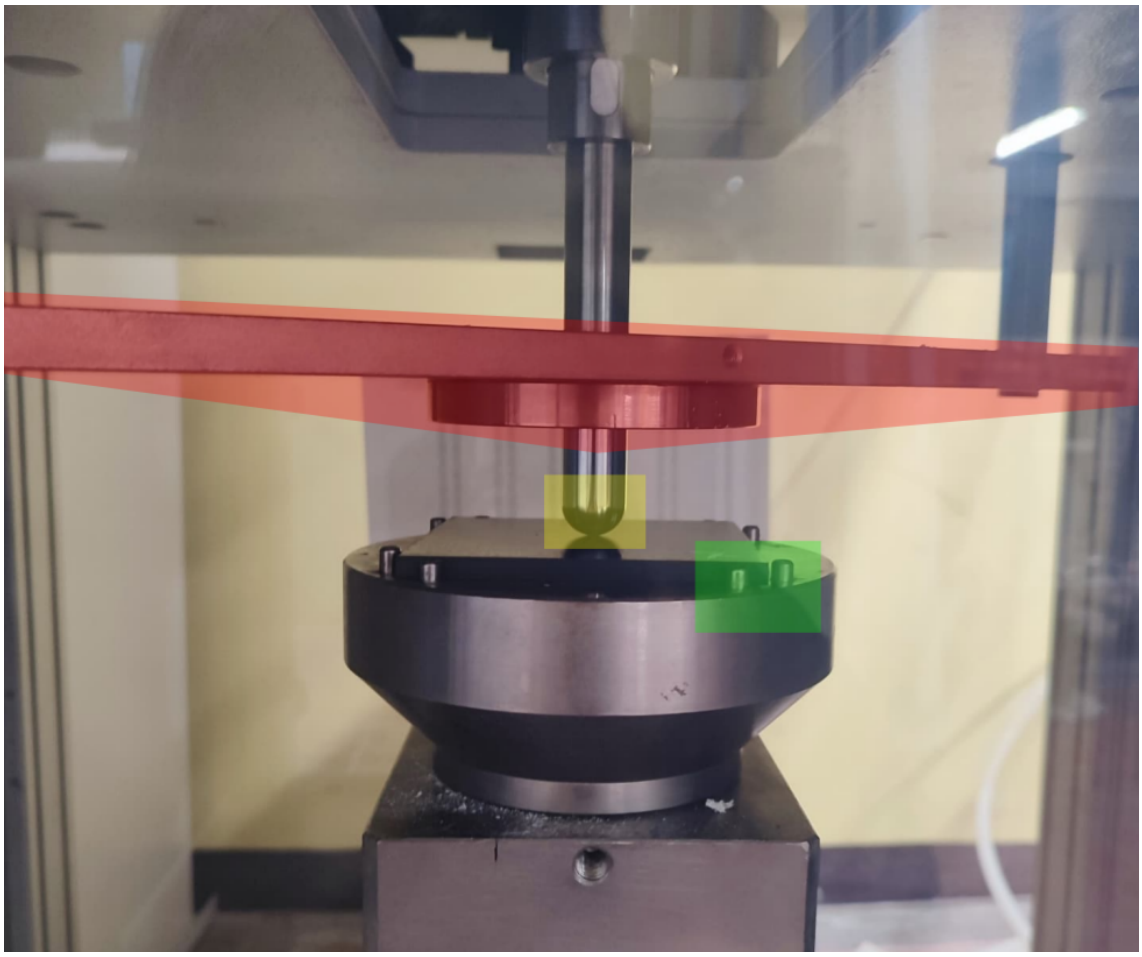

Figure 4.3: Drop weight impact test setup. The hydraulic clamping system is highlighted in red, the hemispherical dart head in yellow, and the alignment pins in green.

4.1.3 Test Results

Figures 4.6 and 4.7 illustrate all the specimens tested during the impact campaign. The fracture patterns observed are consistent with the damage modes classified in the ASTM D7136 standard.

In particular, since all specimens were fully penetrated, the resulting failure mode corresponds to the category defined as *"combined large cracks with fibre breakage and indentation/puncture"* [19]. The analysis of the front and back surfaces highlights a coherent and repeatable fracture morphology: on the impact side, a nearly circular hole is present at the point of contact with the impactor, on the rear face a characteristic cross-shaped crack.

The raw output of the machine consists of the force–time history acquired by the load cell. From this signal, the acceleration of the impactor can be obtained as:

$$a(t) = g - \frac{F(t)}{m} \tag{4.1}$$

where g is the gravitational acceleration, $F(t)$ is the measured contact force, and m is the impactor mass.

The velocity history is then computed by time integration of the acceleration, starting from the initial velocity v_0:

$$v(t) = v_0 + \int_0^t a(\tau)\, d\tau \tag{4.2}$$

The displacement of the dart is obtained as the integral of the velocity:

$$s(t) = \int_0^t v(\tau)\, d\tau \tag{4.3}$$

Finally, the total absorbed energy at the end of the impact event is:

$$E_{\text{tot}} = \int_0^{s_{\max}} F(s)\, ds \tag{4.4}$$

This post-processing procedure, implemented in MATLAB using cumulative trapezoidal integration `cumtrapz`, provides the complete set of histories $a(t)$, $v(t)$, and $s(t)$, while the total absorbed energy E_{tot} was calculated using `trapz` over the full displacement range.

The results of the experimental campaign are reported in the following. As already mentioned, specimen D1 was excluded from the post-processing phase, since it was used as a sacrificial test to verify the experimental setup and calibrate the loading parameters.

Figure 4.4 presents the force–displacement curves for each tested specimen, while Table 4.3 provides a summary of the peak force and the total absorbed energy.

The experimental curves exhibit the characteristic shape of low–velocity impact tests, as defined in ASTM D7136 [19] and discussed in the literature [20, 21]. All specimens were successfully penetrated, resulting in the typical open force–displacement response.

In each case, the initial portion of the curve is linear and represents the elastic response of the material. This stage ends with a first local peak of relatively low force, corresponding to the onset of stiffness degradation. Subsequently, a second non–linear growth phase is observed, leading to the maximum load. After reaching the peak force, the response decreases with a gentler slope: in this region most of the impact energy is dissipated through matrix cracking, fiber breakage, and inter-laminar damage. The force continues to drop progressively until complete specimen

failure, eventually reaching a nearly constant plateau associated with dart sliding and friction against the panel. The latter segment is excluded from the calculation of the absorbed energy.

It can also be observed that increasing the laminate thickness results in a steeper initial rise and an earlier peak load, while the 2 mm specimens display a tendency to sustain forces close to the maximum over a wider deformation range.

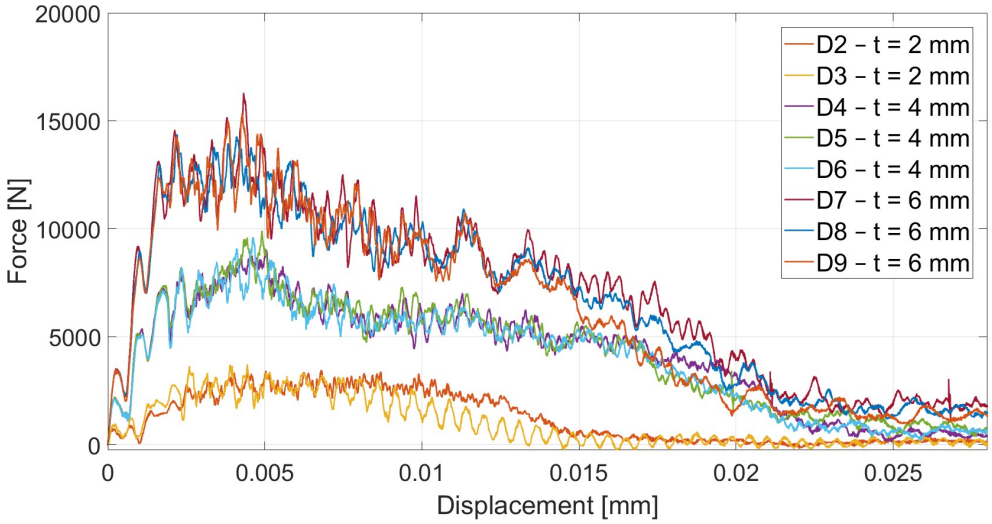

Figure 4.4: Drop weight impact test force-displacement summary chart.

Specimen	**Peak Force [N]**	**Absorbed Energy [J]**
D2	3461	34.1
D3	3722	35.2
D4	9028	121.7
D5	9920	123.0
D6	9961	118.1
D7	16297	214.3
D8	14385	208.2
D9	15358	197.2

Table 4.3: Drop weight impact test results: peak force and total absorbed energy for each specimen.

A further analysis of the results in terms of peak force and absorbed energy highlights the linear dependence of both quantities on the panel thickness within the investigated range, as shown in Figure 4.5.

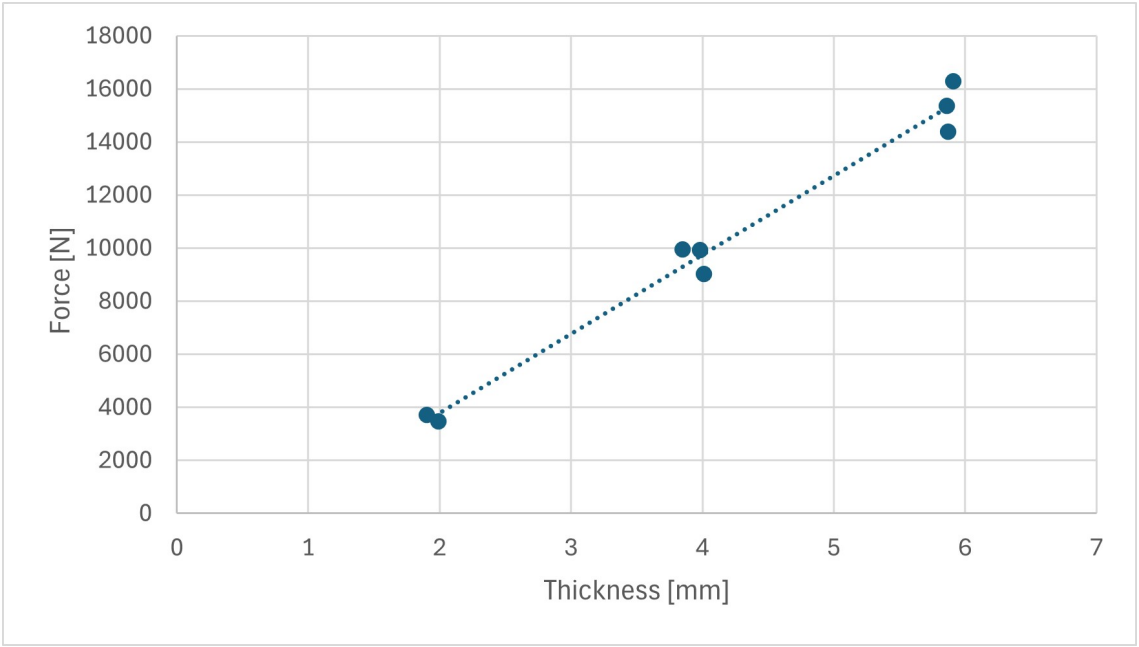

(a)

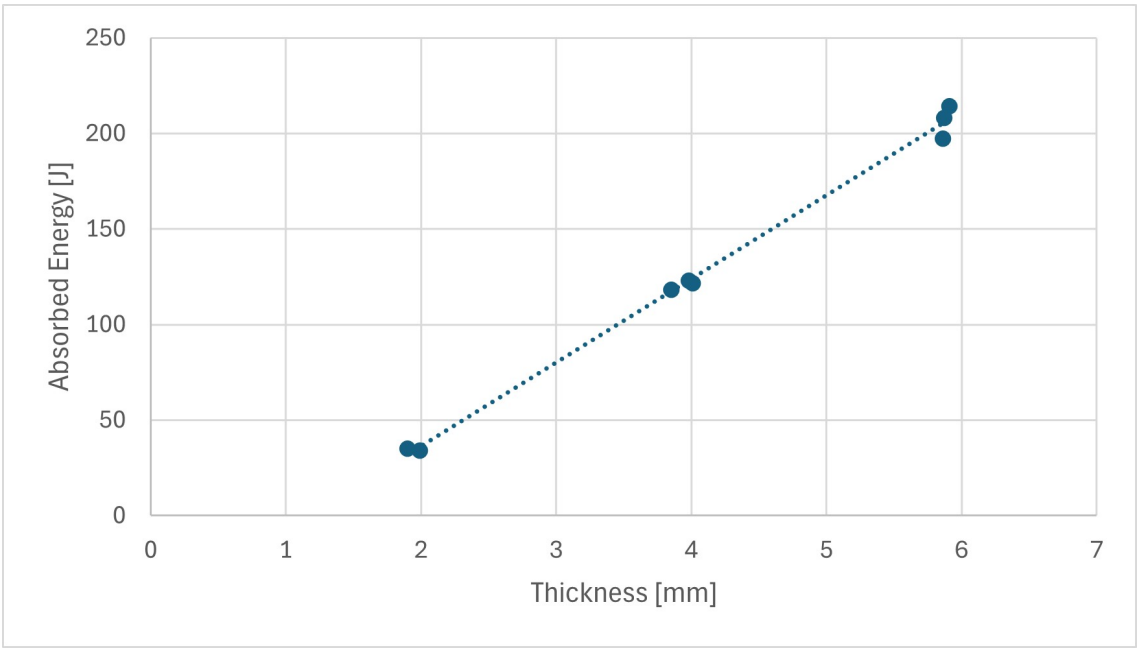

(b)

Figure 4.5: Force (a) and absorbed energy (b) trends for drop weight impact specimens. The results highlight the linear dependence of both quantities on the specimen thickness in the investigated range.

(a)

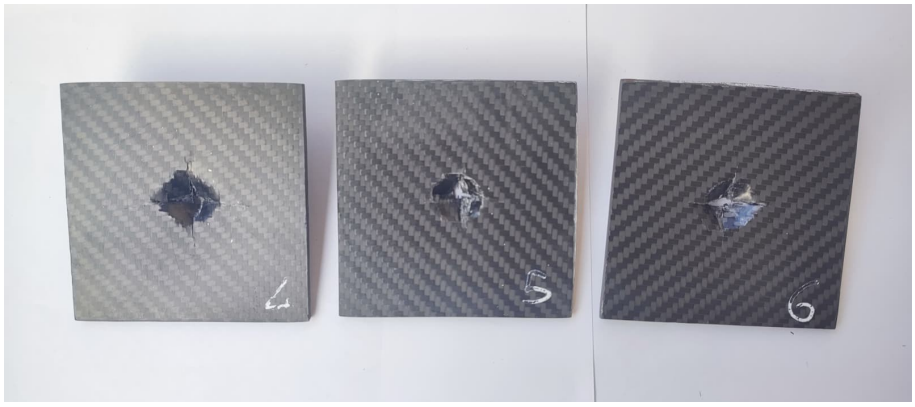

(b)

(c)

Figure 4.6: Impact side of the drop weight specimens after testing: (a) specimens with a nominal thickness of 2 mm; (b) specimens with a nominal thickness of 4 mm; (c) specimens with a nominal thickness of 6 mm.

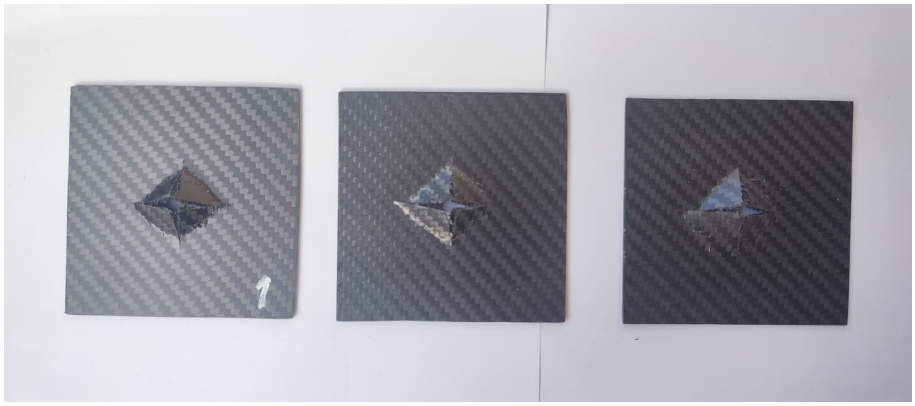

(a)

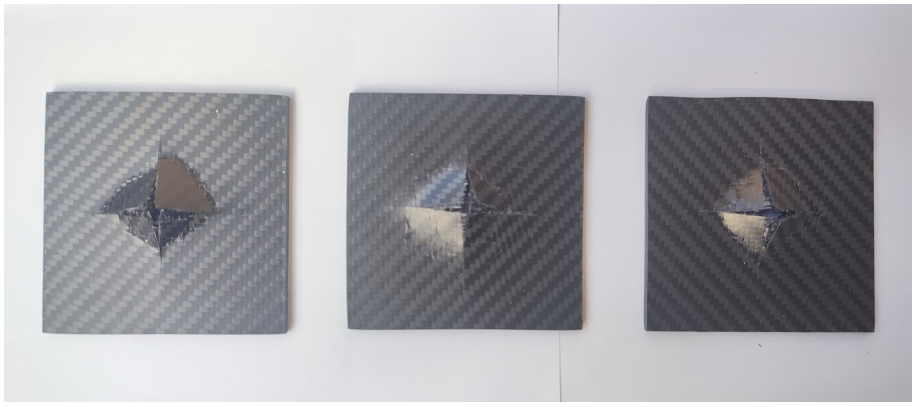

(b)

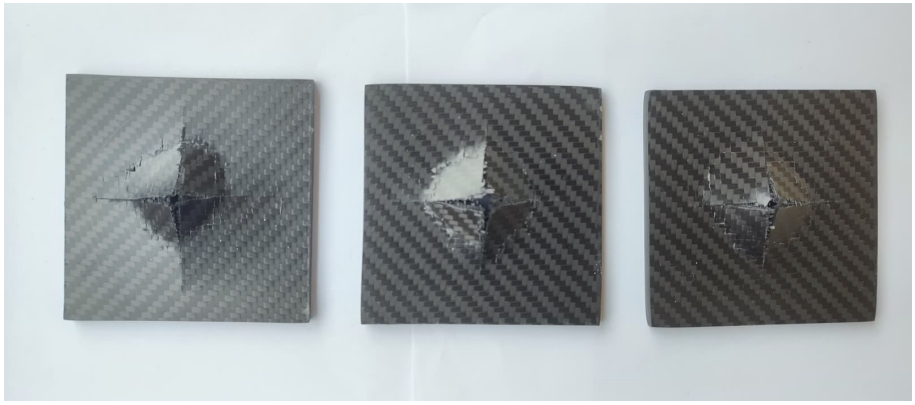

(c)

Figure 4.7: Rear side of the drop weight specimens after testing: (a) specimens with a nominal thickness of 2 mm; (b) specimens with a nominal thickness of 4 mm; (c) specimens with a nominal thickness of 6 mm.

4.2 Drop Weight Impact Model

A quarter–symmetry model was developed in LS-DYNA PrePost, consisting of a reduced representation of the 100 mm × 100 mm test panel. The panel was modelled as a 50 mm × 50 mm quarter section with symmetry boundary conditions, while the impactor was represented by a quarter sphere with a diameter of 20 mm, reproducing the dart head geometry. The fixture was introduced by constraining the panel nodes and defining a circular cut–out with a diameter of 76 mm.

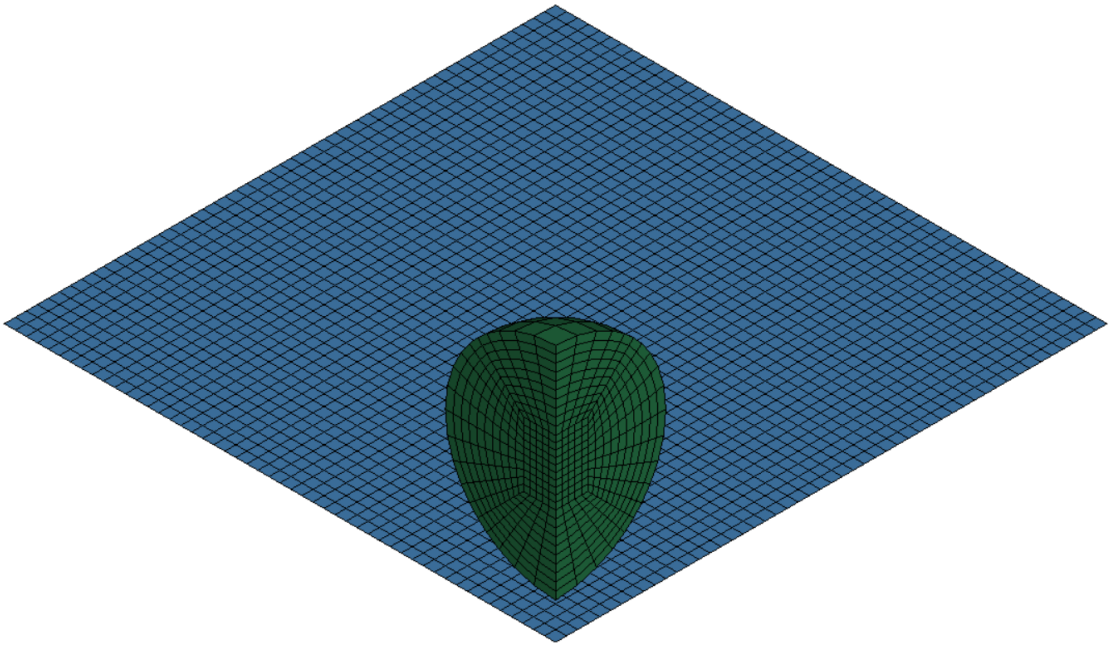

Figure 4.8: Drop weight impact FEM model.

4.2.1 Model Setup

Meshing strategy

The finite element model was composed of shell elements for the CFRP panel and solid elements for the impactor. The entire model was built in LS-DYNA using the `automesher` to generate the shell elements of the plate, and the `shape mesher` to create the spherical impactor, which was subsequently reduced to a quarter by element deletion. The CFRP plate layup was defined through the `PART_COMPOSITE` option, which provides a convenient framework for specifying and modifying the ply sequence.

Element formulation

For the CFRP plate, the fully integrated shell formulation (`ELFORM = 16`) was adopted, whereas the impactor was left with the default solid formulation (`ELFORM = 1`) since it was assigned material model `MAT_020_RIGID`, thus excluding it from the computation.

Contact definition

The interaction between the CFRP panel and the impactor was modeled using an `AUTOMATIC_SURFACE_TO_SURFACE` contact definition. A static coefficient of friction of 0.3 and a dynamic coefficient of 0.2 were specified to account for the sliding behaviour between the two surfaces during impact.

Boundary conditions

As already mentioned, the plate was clamped by constraining the nodes in all six degrees of freedom. A circular cut–out with a diameter of 76 mm was introduced to reproduce the central opening of the experimental fixture, leaving the corresponding nodes free of constraints in order to replicate the actual boundary conditions. Since the model exploits quarter symmetry, only one quarter of the hole is included in the mesh, located at the corner of the 50 mm $\times$ 50 mm panel domain. Model reduction was achieved by imposing symmetry boundary conditions on the lateral nodes of the quarter panel.

The load was applied by assigning an initial velocity of $7\,\mathrm{m\,s^{-1}}$ to the impactor, using the `INITIAL_VELOCITY_GENERATION` card.

4.2.2 Material Cards

The material formulations adopted are the same as those described in Section 3.2.2, with the exception of the honeycomb card, which was not required in this case.

Given the different nature of the test to be simulated, the parameters of the `MAT_054` card were modified accordingly, even though the same base material was considered.

The unit system was consistently defined with mass expressed in grams (g), length in millimetres (mm), and time in milliseconds (ms).

The impactor mass was reproduced by assigning a fictitious density to the `MAT_020_RIGID` card (see Table 4.5). Depending on the specimen thickness under investigation (2 mm, 4 mm or 6 mm), different density values were assigned in order to match the experimental setup reported in Table 4.2. This approach allowed the

replication of all test cases using the same finite element part, without the need for re–meshing.

The `MAT_054` formulation preserves the elastic and shear moduli directly obtained from the characterisation tests, while for the strength parameters it was more appropriate to rely on the datasheet values for tensile and compressive loading.

The parameters reported in rows 4 and 5 of the input card required an extensive calibration process carried out through a trial-and-error procedure. The resulting values differ significantly from those adopted in Section 3.2.2 for the strain-based failure parameters (`DFAIL*`). This difference is not unexpected, as the present model aims to reproduce a different loading scenario, thus requiring parameter values that are consistent with the test under consideration.

	RO	**EA**	**EB**	**(EC)**	**PRBA**	**(PRCA)**	**(PRCB)**
	0.0015	$6.280e+4$	$6.280e+4$				
GAB	**GBC**	**GCA**	**(KF)**	**AOPT**	**2WAY**		
2960	2960	2960		2.0	1.0		
XP	**YP**	**ZP**	**A1**	**A2**	**A3**	**MANGLE**	
			1.0	0.0	0.0		
V1	**V2**	**V3**	**D1**	**D2**	**D3**	**DFAILM**	**DFAILS**
						0.40	0.50
TFAIL	**ALPH**	**SOFT**	**FBRT**	**YCFAC**	**DFAILT**	**DFAILC**	**EFS**
$1e-6$	0.1	0.35	1.0	1.0	0.475	-0.05	
XC	**XT**	**YC**	**YT**	**SC**	**CRIT**	**BETA**	
-583	800	-583	800	128	54		
PEL	**EPSF**	**EPSR**	**TSMD**	**SOFT2**			
				1.0			
SLIMT1	**SLIMC1**	**SLIMT2**	**SLIMC2**	**SLIMS**	**NCYRED**	**SOFTG**	
0.1	0.1	0.1	0.1	0.5		1.0	
LCCX	**LCXT**	**LCYC**	**LCYT**	**LCSC**	**DT**		

Table 4.4: MAT_054 GG200T(T800)-DT120-42 input data for drop weight impact model.

Specimen thickness [mm]	Impactor density [g/mm^3]
2	1.313
4	1.313
6	2.507

Table 4.5: Fictitious density values assigned to the rigid impactor to match the experimental setup for each specimen thickness.

4.2.3 Simulation Results And Solver Settings

The analyses were carried out with the LS-DYNA explicit solver, as already adopted in the previous chapter. No time step control card was applied, whereas an `HOURGLASS` card was introduced. In particular, setting the hourglass control type 8 that activates the full projection warping stiffness, which is applicable to the type 16 and -16 fully integrated shell element.

The simulation results were analysed in terms of force–displacement curves, peak force and absorbed energy, and compared with the average experimental response for each specimen thickness. Given the limited number of specimens tested for each configuration and the very low scatter observed among the experimental curves, the mean response was considered representative of the experimental behaviour.

From the average of the experimental values of peak force and absorbed energy reported in Table 4.3, the corresponding quantities obtained from the numerical models were compared in order to evaluate the error of the simulations with respect to the physical tests. Table 4.6 reports, for each specimen thickness, the numerical peak force and absorbed energy, the percentage error with respect to the experimental averages, and the coefficient of determination R^2 used to quantify the representativeness of the numerical force–displacement response with respect to the average experimental curve, as also highlighted in Figure 4.9.

The largest discrepancy was observed for the absorbed energy in the thinnest laminate, where the model overestimates the experimental value by approximately 12%. This deviation was considered acceptable since, as the laminate thickness increases towards values more relevant for the AIP design, the error decreases and the model tends to slightly underestimate the absorbed energy, thus providing a conservative prediction in terms of safety.

Regarding the peak forces, the model exhibits a very accurate estimation for thin laminates, while for thicker ones, a tendency to underestimate the maximum load is observed. Overall, the model can be regarded as successful, as it is capable of predicting with satisfactory accuracy a wide range of laminate thicknesses. Further-

more, the analysis of the determination coefficient confirms an excellent agreement between the experimental and numerical force–displacement curves.

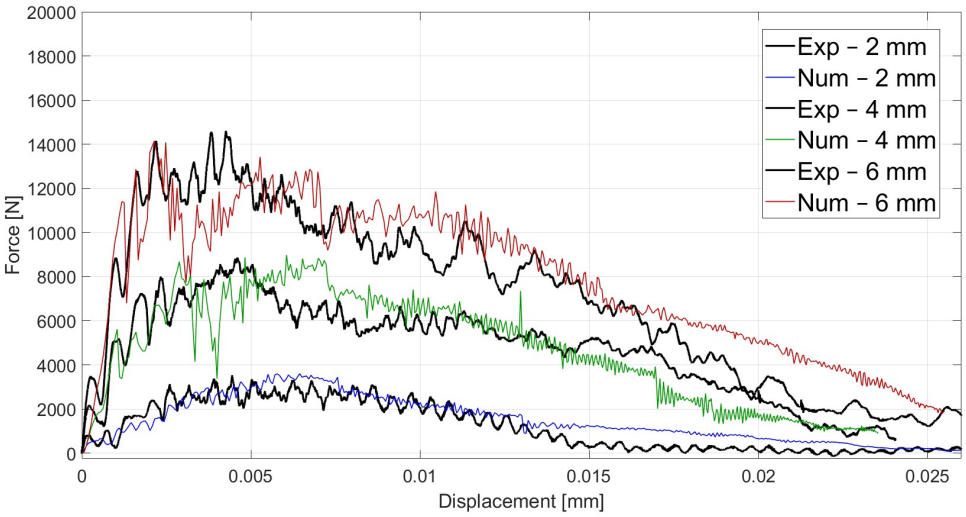

Figure 4.9: Comparison between experimental and numerical force–displacement curves for the three investigated thicknesses (2 mm, 4 mm and 6 mm).

Thickness [mm]	$F_{\mathbf{max,num}}$ [N]	$\mathbf{err}_F$ [%]	$E_{\mathbf{abs,num}}$ [J]	$\mathbf{err}_E$ [%]	R^2
2	3603	0.3	38.8	12.0	0.80
4	8977	−6.8	111.3	−8.0	0.79
6	14 610	−4.9	201.4	−2.5	0.84

Table 4.6: Comparison between numerical and experimental results. Simulated peak force and absorbed energy, relative error with respect to experimental averages, and coefficient of determination R^2.

4.3 Integrated Monolithic Impact Assembly Model

4.3.1 Model Objectives

Starting from the configuration presented in Section 3.3, the investigation of the alternative monolithic solution was carried out by replacing the sandwich architecture with the fully composite design. The parameters of the material card are the one calibrated as described in Section 4.2. The boundary conditions and contact definitions were kept identical to those applied in the sandwich model; the reader is referred to Section 3.3.1 for further details.

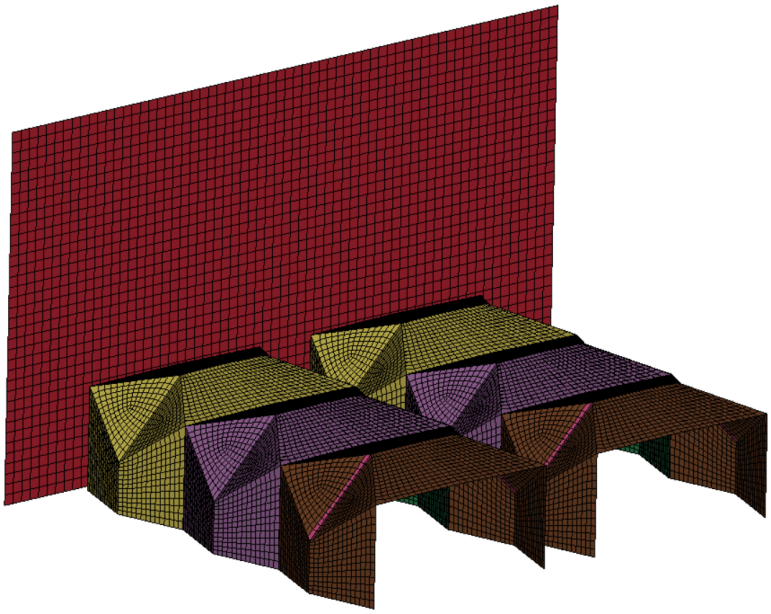

Figure 4.10: Integrated FEM model of the IA from Patruno combined with the monolithic AIP derived from the drop weight impact.

The objectives of the monolithic model can be summarised as follows:

- identify the suitable thickness and number of plies for the AIP structure;
- ensure structural integrity of the assembly during the crash event;
- limit the permanent deformation of the attenuator to less than the 25 mm threshold prescribed by the regulations;
- achieve these safety targets while maintaining a reduced mass compared to the already adopted solutions.

If these requirements are met, the design phase of the AIP can be considered complete and the configuration valid for implementation in the final assembly.

4.3.2 Simulation Results And Solver Settings

The numerical analyses were carried out with the LS-DYNA explicit solver, with continuous monitoring of the energy balance that included both dissipation and hourglass contributions. To prevent spurious hourglass modes in the CFRP skins, hourglass control type 8 was adopted, which introduces the full projection warping stiffness available for shell formulations 16 and -16.

The simulation was terminated once the wall started to rebound, following the complete crushing of the IA.

The results were analysed in terms of maximum principal stresses on the average surface of the AIP panel. The highest stress value, equal to 378 MPa, was recorded at approximately 16 ms (see Figure 4.11).

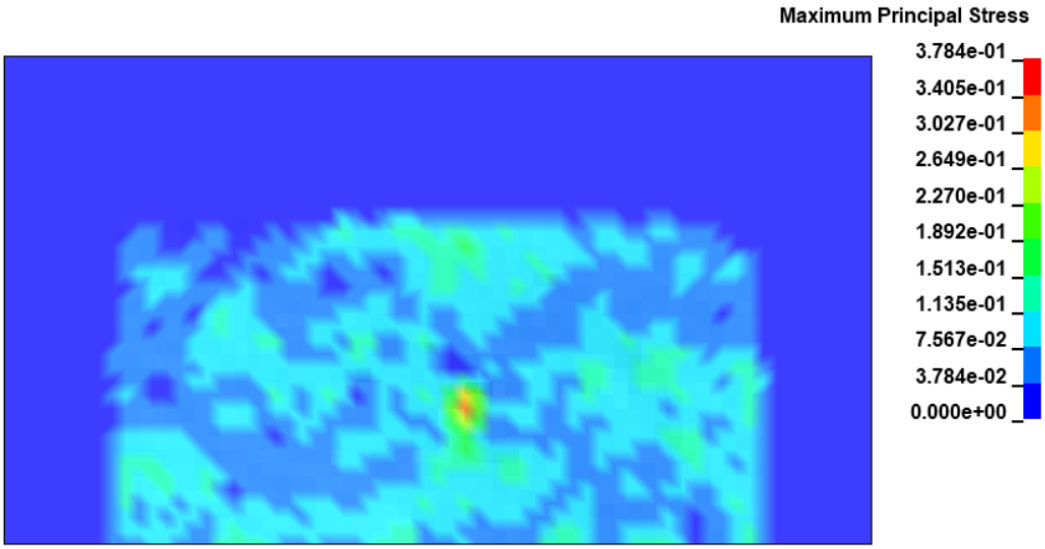

Figure 4.11: Heat map showing the maximum principal stress distribution in GPa for the monolithic AIP panel.

The time–displacement response of the node exhibiting the maximum deflection is shown in Figure 4.12. The results confirm that the maximum displacement remains well below the regulatory threshold of 25 mm, thus satisfying the integrity requirements for the AIP.

Figure 4.13, which illustrates the maximum out-of-plane displacement field, highlights the significant bending load that the AIP must sustain as a consequence of the prescribed boundary conditions.

The analysis indicated that the suitable configuration for the T800 CFRP prepreg consists of 30 plies, corresponding to a total thickness of 6.9 mm and a weight of 770 g. No optimization was performed with respect to ply orientation, as all plies were aligned at 0°. Consequently, this outcome represents a conservative estimate and could be further improved in future studies by exploring different layup strategies.

Table 4.7 reports the summary of the most relevant outcomes obtained for the newly developed monolithic configuration.

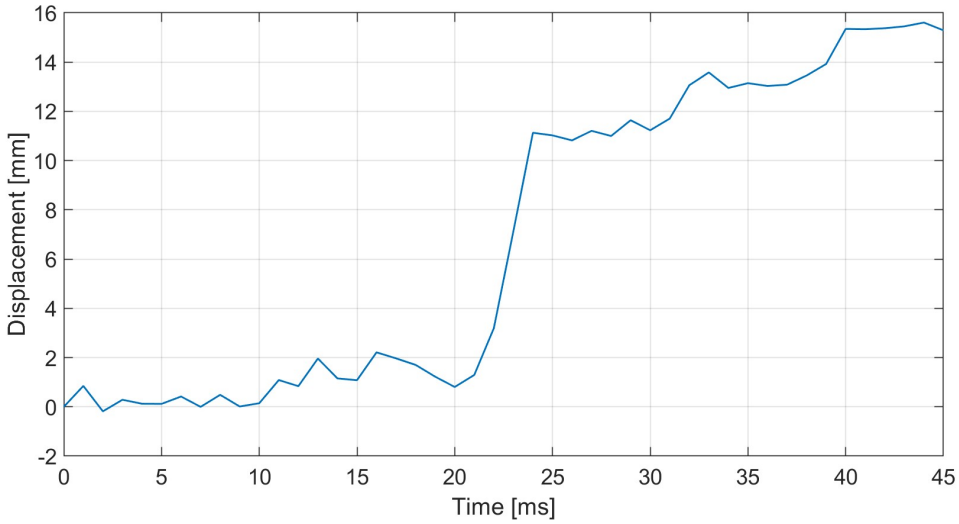

Figure 4.12: Time-displacement response of the monolithic AIP during the crash simulation. The curve highlights the maximum node deflection.

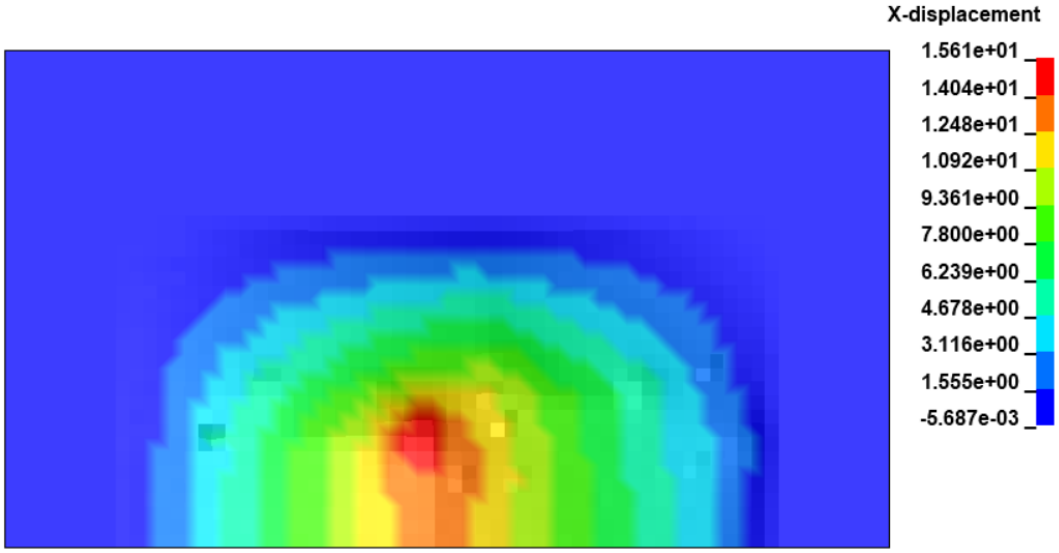

Figure 4.13: Heat map showing the maximum x displacement distribution in millimeters for the monolithic AIP panel.

Layup configuration	$[0°]_{30}$
Total thickness	6.9 mm
Max displacement	15.6 mm
AIP weight	770 g

Table 4.7: Summary of the monolithic AIP design relevant results.

Chapter 5

Results and Conclusions

5.1 Results

Building on the results presented in Chapter 4, a direct comparison can be drawn between the state-of-the-art solutions and the design proposed here.

First, the initial hypothesis is confirmed: the load case generated by the origami CFRP IA is incompatible with the mechanical behaviour of a sandwich panel. The weak link in the load-path stiffness is the aluminium honeycomb core in out-of-plane shear, which inevitably triggers premature failure. Removing the core and adopting a monolithic solution was therefore a necessary step.

From a numerical perspective, the new design offers superior mechanical performance while also reducing mass. This suggests that the proposed approach is better suited to the present case study, as it combines structural efficiency with weight savings.

Drop-weight impact tests corroborate these findings: increasing the face-sheet thickness yields an approximately linear improvement in resistance to localised impact loads (Figure 4.5a), identifying thickness as the primary design driver. This evidence, together with the simulation results, guided the final selection of a 0° laminate with 30 pliers, for a total thickness of approximately 7 mm. Future work may target ply-angle optimisation to further reduce mass while preserving performance. Note that the observed linearity was verified only within the 2 mm to 6 mm interval, whereas the final AIP thickness lies slightly outside this range.

Despite the reduction in flexural inertia associated with the lower thickness, the monolithic configuration still complies with the residual deformation limits mandated by the regulations.

The weight advantage is particularly significant. Based on the current AIP geometry adopted by the team (Figures 1.2 and 1.4), the masses of the steel, alu-

minum and monolithic variants were estimated from the density of the material and the weight of the area of the fabric, while the sandwich variant was measured by weighing. The comparison is summarised in Table 5.1. The results highlight the clear benefit of the monolithic CFRP design, which achieves the lowest mass while maintaining regulatory compliance.

AIP Design	**Mass [g]**	**Weight Reduction [%]**
Steel	1519	+48
Aluminium	1398	+36
Sandwich	1026	—
CFRP monolithic	774	-25

Table 5.1: Comparison of AIP mass for different design solutions.

It is also worth noting that the previous sandwich design suffered from additional drawbacks. The adhesive bonding of inserts increased the final mass, yielding the value reported in Table 5.1. This effect is absent in the monolithic solution, where the only constituent is the CFRP prepreg and the final mass can be reliably estimated from the fabric areal weight.

Finally, the manufacturing process itself is a further strength of the proposed design. Producing a flat laminated panel is substantially simpler than building a sandwich component with multiple inserts (nine in the current design). The need to position and bond these inserts carefully—to guarantee proper fastening to the FBH—is eliminated in the monolithic approach, reducing both complexity and potential sources of error.

In summary, the proposed monolithic CFRP AIP combines superior mechanical performance, full regulatory compliance, substantial weight reduction, and notable manufacturing simplicity.

5.2 Conclusions

The research presented in this thesis focused on the design of innovative structural solutions for the Anti-Intrusion Plate within the Impact Assembly of Formula SAE vehicles. The work was motivated by the crash test results of the Squadra Corse PoliTo origami-shaped composite Impact Attenuator, where premature perforation of the sandwich Anti-Intrusion Plate highlighted the need for improved crashworthiness of the subsystem.

An integrated experimental–numerical methodology was adopted.

The first stage involved the mechanical characterization of the selected composite system through tensile and in-plane shear tests.

The second stage focused on the sandwich Anti-Intrusion Plate, experimentally tested under perimeter shear loading and numerically reproduced through quarter-symmetry FEM models. Both tests and simulations confirmed that the honeycomb core configuration, while lightweight and stiff under distributed loads, is highly vulnerable to localised concentrated stresses. The integrated crash model, coupling the origami Impact Attenuator with the sandwich Anti-Intrusion Plate, reproduced the experimentally observed penetration failure, thus confirming the inadequacy of this architecture for Formula SAE crashworthiness requirements.

To overcome these limitations, the research then developed a monolithic full-CFRP Anti-Intrusion Plate. A drop weight impact campaign demonstrated that the monolithic design exhibits a stable and progressive damage evolution, with peak force and absorbed energy scaling with thickness. The corresponding LS-DYNA models, based on calibrated MAT_054 formulations, accurately captured the force–displacement response across the investigated thicknesses. When integrated into the Impact Assembly crash model, the monolithic Anti-Intrusion Plate successfully prevented penetration while meeting the Formula SAE regulatory limits. Importantly, this solution also achieved a significant mass reduction compared to metallic and sandwich alternatives.

Overall, the thesis demonstrates that the monolithic CFRP Anti-Intrusion Plate configuration represents a viable alternative for Formula SAE vehicles. The findings highlight the importance of coupling material characterization with structural simulations, enabling predictive crash design.

Future efforts will focus on exploring hybrid laminates (e.g., aramid–carbon) to tailor the impact response, validating the monolithic design through the full-scale crash tests prescribed by the Formula SAE regulations, and optimizing layup sequences to further reduce mass while maintaining performance.

Bibliography

[1] SAE International. About sae formula events. https://www.sae.org/attend/student-events/about-formula, 2024.

[2] Formula Student Germany. Formula student germany 2025 rules (version 1.1). https://www.formulastudent.de/fileadmin/user_upload/all/2025/rules/FS-Rules_2025_v1.1.pdf., 2025.

[3] Formula SAE. Standard impact attenuator technical drawing. https://www.fsaeonline.com/cdsweb/app/NewsItem.aspx?NewsItemID=cfaab406-3dda-45d6-bce9-fc100e0fa4a0, 2023.

[4] Moisey B. Shkolnikov. Honeycomb modelling for side impact moving deformable barrier (mdb). Proceedings of the 7th International LS-DYNA Users Conference https://lsdyna.ansys.com/wp-content/uploads/attachments/Session_7-1.pdf, 2002.

[5] Luca Patruno. Design of an origami shaped composite structure with application to a race car crash absorber. Master's thesis, Politecnico di Torino, 2023.

[6] A. Ciampaglia, D. Fiumarella, C. Boursier Niutta, R. Ciardiello, and G. Belingardi. Impact response of an origami-shaped composite crash box: Experimental analysis and numerical optimization. Composite Structures, 256:113093 https://doi.org/10.1016/j.compstruct.2020.113093, 2021.

[7] Paolo Feraboli, Bonnie Wade, Francesco Deleo, Mostafa Rassaian, Mark Higgins, and Alan Byar. Ls-dyna mat54 modeling of the axial crushing of a composite tape sinusoidal specimen. Composites Part A: Applied Science and Manufacturing, 42(11):1809–1825 https://doi.org/10.1016/j.compositesa.2011.08.004, 2011.

[8] Bonnie Wade, Paolo Feraboli, Morgan Osborne, and Mostafa Rassaian. Simulating laminated composite materials using ls-dyna material model mat54:

Single-element investigation. Technical Report DOT/FAA/TC-14/19, U.S. Department of Transportation, Federal Aviation Administration, William J. Hughes Technical Center, Atlantic City International Airport, NJ, February 2015. https://www.researchgate.net/publication/322152587.

[9] Ravin Garg, Iman Babaei, Davide Salvatore Paolino, et al. Predicting composite component behavior using element level crashworthiness tests, finite element analysis and automated parametric identification. Materials https://doi.org/10.3390/ma13204501, 2020.

[10] RP Proto. Carbon fiber material overview. https://www.rpproto.com/carbon-fiber-material, 2023.

[11] Delta-Preg S.p.A. Product selector. https://www.delta-preg.com/product-selector/, 2023.

[12] ASTM International. Standard test method for tensile properties of polymer matrix composite materials.

[13] ASTM International. Standard test method for in-plane shear response of polymer matrix composite materials by tensile test of a ±45° laminate.

[14] Ansys. Ls-dyna keyword user's manual, volume 2: Material models. https://lsdyna.ansys.com/manuals/, 2024. Release R15.

[15] R. A. Cutting, A. J. Favaloro, and J. E. Goodsell. A novel post-processing method for progressive failure analysis of brittle composite compression. Journal of Composite Materials, 56(19):3029–3047 https://journals.sagepub.com/doi/10.1177/00219983221101985, 2022.

[16] A.S.M. Ayman Ashab et al. Finite element analysis of aluminum honeycombs subjected to dynamic indentation and compression loads. *Materials*, 9:162, 2016. https://doi.org/10.3390/ma9030162.

[17] Ansys. Ls-dyna keyword user's manual, volume 1. https://lsdyna.ansys.com/manuals/, 2024. Release R15.

[18] R. Ciepielewski and D. Miedzińska. A study of aluminum honeycomb structures under dynamic loading, with consideration given to the effects of air leakage. *Materials*, 16:2211, 2023. https://www.mdpi.com/1996-1944/16/6/2211.

[19] ASTM International. Standard test method for measuring the damage resistance of a fiber-reinforced polymer matrix composite to a drop-weight impact event.

[20] Zhen Wang and Guijun Xian. Impact performances of fiber reinforced polymer composites and cables: A review. *Composite Structures*, 319:117128, 2023. https://doi.org/10.1016/j.compstruct.2023.117128.

[21] Xiaogang Liu, Weichen Kong, Siqi Song, and Anni Wang. Impact properties and damage assessment of unidirectional aramid/carbon fiber hybrid reinforced polymer composites. *Thin-Walled Structures*, 209:112898, 2025. https://doi.org/10.1016/j.tws.2024.112898.